

MODELING THE ROOT PROTOPHLOEM UNLOADING NETWORK

By

GRAYSON PIERCE OSTERMEYER

A thesis submitted in partial fulfillment of
the requirements for the degree of

MASTER OF SCIENCE IN PLANT BIOLOGY

WASHINGTON STATE UNIVERSITY
School of Biological Sciences

MAY 2019

© Copyright by GRAYSON PIERCE OSTERMEYER, 2019
All Rights Reserved

© Copyright by GRAYSON PIERCE OSTERMEYER, 2019
All Rights Reserved

To the Faculty of Washington State University:

The members of the Committee appointed to examine the dissertation/thesis of
GRAYSON PIERCE OSTERMEYER find it satisfactory and recommend that it be accepted.

Michael Knoblauch, Ph.D., Chair

Asaph Cousins, Ph.D.

Hans-Henning Kunz, Ph.D.

MODELING THE ROOT PROTOPHLOEM UNLOADING NETWORK

Abstract

by Grayson Ostermeyer, M.S.
Washington State University
May 2019

Chair: Michael Knoblauch

Phloem is the vascular system that carries out long-distance transport of important biological compounds in all higher plants. During photosynthesis, light-exposed green tissues synthesize sugar molecules that can be broken down in other regions of the plant to drive processes like functional metabolism, organ growth, and nutrient storage. The structural conduit that forms a channel linking photosynthetic source tissues to recipient sink tissues is composed of interconnected sieve tube elements. Flow of energy-rich, carbon-based molecules through this tube is a prominent research focus of plant scientists because sink organs include many economically important agricultural products, such as fruits and tubers. The terminal segment of phloem in plant roots, the protophloem, acts as a platform through which assimilates unload from the phloem vasculature to supply the actively growing root tip with biochemical fuel. Cellular organization of the protophloem tissue exhibits predictable patterns in plant roots and are characteristic in each species. Outflow of vascular cargo into adjacent cells of the root protophloem occurs through sub-microscopic pores called plasmodesmata that link the internal contents of nearly every cell in the plant body. Plasmodesmal morphology has a considerable

effect on the symplasmic flow rate and regulates the unloading capacity of roots. Previous research efforts have described variations in the shape of plasmodesmata as simple or branched based on the number of intercellular connections formed by the pore structure. Recently identified plasmodesmata at the interface between protophloem sieve elements and phloem pole pericycle cells demonstrated a funnel shape, possibly endowing this pore type with enhanced assimilate unloading potential. Our research efforts began by refining a sample preservation protocol for angiosperm roots and illuminating species-specific variations in the tissue structure of protophloem using transmission electron microscopy. We then proceeded to model flow dynamics in plasmodesmata using electron tomography and finite element analysis, producing the first 3D reconstructions of plasmodesmata in the process. Our imaging workflow and flow analysis approach may be useful in experiments aimed at manipulating plasmodesma geometry to accommodate greater flux of assimilates into sink crops, thereby increasing food availability for a growing world population.

TABLE OF CONTENTS

	Page
ABSTRACT.....	iii
LIST OF TABLES.....	vii
LIST OF FIGURES	viii
DEDICATION.....	ix
CHAPTER	
CHAPTER ONE: ON BOTANY, PHLOEM, AND IMAGING PLANTS	1
THE SCIENTIFIC STUDY OF PLANTS.....	1
THE PHLOEM	3
PLASMODESMATA	7
FLUID MECHANICS IN PLANTS	9
PHLOEM UNLOADING IN THE ROOTS OF <i>ARABIDOPSIS THALIANA</i>	11
PRESERVATION OF PLANT TISSUE	12
IMAGING PLANTS.....	16
MY RESEARCH	18
CHAPTER TWO: MODELING THE STRUCTURE AND FLOW DYNAMICS OF PLASMODESMATA FROM THE UNLOADING ZONE OF ANGIOSPERM ROOTS	26
ABSTRACT.....	27
INTRODUCTION	28
RESULTS	32
DISCUSSION	42
MATERIALS AND METHODS.....	45

AUTHOR CONTRIBUTIONS.....	47
ACKNOWLEDGEMENTS	48
REFERENCES	73

LIST OF TABLES

	Page
Table 2-1: A comparison of funnel plasmodesmata dimensions in various roots relative to <i>Arabidopsis thaliana</i>	49

LIST OF FIGURES

	Page
Figure 1-1: Subcellular features of sieve elements	20
Figure 1-2: A schematic representation of the components present in a typical plasmodesma	21
Figure 1-3: Workflow for preparing biological samples for imaging by light and electron microscopy	22
Figure 1-4: A schematic diagram of phloem-mediated assimilate transport pathways	23
Figure 1-5: A schematic diagram of functional regions related to phloem elongation and assimilate unloading in <i>Arabidopsis thaliana</i> roots.....	24
Figure 1-6: Ultrastructural organization of vasculature observed in cross section through the root unloading zone of <i>Arabidopsis thaliana</i>	25
Figure 2-1: Cross sectional view of the root unloading zone of <i>Triticum aestivum</i>	50
Figure 2-2: Cross sectional view of the root unloading zone of <i>Oryza sativa</i>	51
Figure 2-3: Cross sectional view of the root unloading zone of <i>Nicotiana tabacum</i>	52
Figure 2-4: Cross sectional view of the root unloading zone of <i>Medicago sativa</i>	53
Figure 2-5: Cross sectional view of the root unloading zone of <i>Ipomoea nil</i>	54
Figure 2-6: Cross sectional view of the root unloading zone of <i>Solenostemon scutellarioides</i>	55
Figure 2-7: Cross sectional view of the root unloading zone of <i>Catalpa speciosa</i>	56
Figure 2-8: Cross sectional view of the root unloading zone of <i>Quercus rubra</i>	57
Figure 2-9: Plasmodesma varieties present in the root protophloem sieve element cell walls of <i>Triticum aestivum</i>	58
Figure 2-10: Plasmodesma varieties present in the root protophloem sieve element cell walls of <i>Oryza sativa</i>	59

Figure 2-11: Plasmodesma varieties present in the root protophloem sieve element cell walls of <i>Nicotiana tabacum</i>	60
Figure 2-12: Plasmodesma varieties present in the root protophloem sieve element cell walls of <i>Medicago sativa</i>	61
Figure 2-13: Plasmodesma varieties present in the root protophloem sieve element cell walls of <i>Ipomoea nil</i>	62
Figure 2-14: Plasmodesma varieties present in the root protophloem sieve element cell walls of <i>Solenostemon scutellarioides</i>	63
Figure 2-15: Plasmodesma varieties present in the root protophloem sieve element cell walls of <i>Catalpa speciosa</i>	64
Figure 2-16: Plasmodesma varieties present in the root protophloem sieve element cell walls of <i>Quercus rubra</i>	65
Figure 2-17: Variation in independent measurements performed on plasmodesmata	66
Figure 2-18: Conceptual approach to modeling aperture diameters in funnel plasmodesmata using micrographs that contain obscure and incomplete information	67
Figure 2-19: Distribution of predicted border lengths present at the margins of a large number of funnel plasmodesmata funnel apertures	68
Figure 2-20: Three-dimensional reconstruction of a simple plasmodesma at the protophloem sieve element-metaphloem sieve element cell wall interface in <i>Nicotiana tabacum</i>	69
Figure 2-21: Three-dimensional reconstruction of a simple plasmodesma at the protophloem sieve element-phloem pole pericycle cell wall interface in <i>Nicotiana tabacum</i>	70
Figure 2-22: Three-dimensional reconstruction of a simple plasmodesma at the protophloem sieve element-phloem pole pericycle cell wall interface in <i>Triticum aestivum</i>	71

Figure 2-23: Laminar flow through a *Triticum aestivum* funnel plasmodesma.....72

Dedication

This thesis is dedicated to the people at the Franceschi Microscopy and Imaging Center at Washington State University for their roles in advancing student knowledge. I am particularly grateful for the years of mentorship provided by Michael Knoblauch and Winfried Peters. Their support was a constant source of inspiration and for that I owe them a debt of gratitude.

CHAPTER ONE: ON BOTANY, PHLOEM, AND IMAGING PLANTS

The Scientific Study of Plants

Human interest in plants developed long before the first written records because plant-based products provided the nutrients, clothing fibers, weapons, and shelter-building materials needed for our species to survive (Barham and Mitchell, 2008). Recognition of the natural therapeutic properties offered by certain plants prompted premodern societies to embrace herbalism – the practice of studying and cultivating plants to apply their pharmacological elements towards practical enterprises like medicine (Sumner, 2000). Plants are also common subjects in religious and oral traditions around the world due to their subjective attributes of durability, fruitage, and capacity for sustained growth (Bennett, 1994). Reorganization of human society from foraging to primarily agrarian communities, where farming and land-ownership account for most of a family's income, fundamentally reshaped social power dynamics by introducing wealth-based class systems and strict gender norms (Brenner, 1976). More recently, revolutions in agriculture have been spawned by advances in industrial technology and a greater understanding of how plants are put together and function (Stern et al., 2003; Grinin, 2007). The resulting increases in agricultural productivity have made possible staggering growth of the human population. The world population in 0 CE, for example, is estimated to have been about 188 million people – an increase from the 2 million people alive during the Stone Age over the time span of 10,000 years (Roser and Ortiz-Ospina, 2017). Yet, during the relatively brief 200 years between 1800 and 2000 CE, the human population swelled by over 5 billion people (Roser and Ortiz-Ospina, 2017). This story sheds light on the bearing that plants have had in shaping human history, and hint and their promise as instruments of change.

While humans have long been curious about how to improve plant output to suit their needs, the turning point in realizing how to translate their potential to boost human livelihood hinged on new ways of thinking ushered in during the scientific revolution beginning in the 16th century (Morton, 1981). The value of scientific inquiry lies in the empirical approach of acquiring knowledge using the scientific method – a systematic way of testing hypotheses through rigorous experimentation (Cohen, 2013). In science, prudent skepticism about the true nature of a system, or what one claims to be fact, reduces the perpetuity of improper conclusions (Cohen, 2013). Accordingly, well-behaved hypotheses must be falsifiable – that is, an outcome must exist which disproves the predictions modeled in a proposition (Cohen, 2013). These principles drive plant scientists to design elegant experiments aimed at describing natural systems, which are often obscured by practical barriers. The internal, nutrient-conducting vasculature of plants is one example.

Botany is the scientific study of plants (Stern et al., 2003). As a multidisciplinary field, the scope of botanical research themes include plant-pest interactions, hormone signaling pathways, and developmental anatomy (Stern et al., 2003). Applied science practitioners are interested in designing plants with disease resistance and enhanced plant investment in crop production (Savary et al, 2012). Projects such as these are vital endeavors if world agricultural output will be meet the food consumption demands of the more than 11 billion people projected to inhabit our planet by 2100 (Roser and Ortiz-Ospina, 2017). Investigations in pure science are equally indispensable. Concealed in the fine structure of known tissues, such as the phloem of vascular plants, are biological targets with potentially important implications in regulating plant growth and development.

The Phloem

Vascular plants (tracheophytes) form a large and diverse subclade within the plant kingdom (Christenhusz, 2016). Tracheophytes include species that are both abundant and widespread, including all trees, vines, shrubs, and economically important crops (Christenhusz, 2016). Vascular plants have green, light-exposed tissues visible on their aerial organs, especially in leaves, where they are most concentrated (Christenhusz, 2016). The color of leaves and stems offers a perceptual clue to the underlying physiology of plants in that green light corresponds to the segment of the light spectrum that is reflected from these tissues (Terashima et al., 2009). Chlorophyll molecules present in the chloroplasts of plant cells in these green tissues are capable of harvesting electromagnetic radiative energy of other regions of the light spectrum, such as those that are perceptually blue and red, to drive a photochemical process called photosynthesis (Terashima et al., 2009). In photosynthesis, molecules of carbon dioxide are assimilated with water molecules to produce glucose and gaseous oxygen (Haupt-Herting and Fock, 2002). The glucose produced in this reaction can subsequently be broken down and coupled to otherwise energetically unfavorable reactions involved in the metabolism and synthesis of cellular components (Haupt-Herting and Fock, 2002). The oxygen byproduct of photosynthesis supplies an input for organisms that derive their energy from cellular respiration, a chemical reaction in organisms where oxygen and glucose are consumed to produce water and carbon dioxide (Haupt-Herting and Fock, 2002). By facilitating the production of oxygen and energy-rich organic substrates that other species consume, plants provide ecological stability (Mellinger and McNaughton, 1975). Vascular plants are particularly well-suited to photosynthetic turnover and carry out almost all of the primary production in terrestrial environments (Roy, 2001).

The bioenergetic advantages offered by photosynthesis are not unique to vascular plants (Raven, 2003). Rather, the evolution of a microfluidics system capable of efficiently redistributing the soluble products of photosynthesis to other parts of the plant body endowed vascular plants with a strategy to overcome diffusion-mediated size limitations (Raven, 2003). Physiological gradients imposed by the separation of photosynthetic source and sink tissues reveal how vascular plants achieve cellular division of labor. To this end, plant cells at topical, light-exposed surfaces generally dedicate their metabolism to carbon assimilation (De Oliveira Dal'Molin, 2015). By channeling their nutrients to non-photosynthetic cells such as those of the meristems, plants repurpose these organic compounds to fuel processes like root growth (De Oliveira Dal'Molin, 2015).

Phloem is the plant tissue that mediates the translocation of photoassimilates, as well as other macromolecules like nucleic acids, lipids, and proteins (Evert and Eichhorn, 2006). Along with xylem, the water-conducting plant tissue, the presence of phloem is a defining criterion of vascular plants (Christenhusz, 2016). Sieve elements are cells that provide a narrow conduit for nutrient transport (Knoblauch and van Bel, 1998). Companion cells are specialized parenchyma cells that sustain their ontogenetically-related sieve element neighbors (Knoblauch and van Bel, 1998). The sieve element and neighboring companion cell are often referred to as the sieve element-companion cell complex (SECCC) due to the functionally integrated domain that they form (Evert and Eichhorn, 2006). Metabolic support from companion cells is vital for sieve elements because they lose their nucleus, cytoplasm, vacuole, ribosomes, Golgi bodies, and cytoskeleton at maturity in order to facilitate fluid conduction (Evert and Eichhorn, 2006). Endoplasmic reticulum, mitochondria, plastids, and a plasma membranes are retained at sieve element maturity (Evert and Eichhorn, 2006). In addition to sieve elements and companion cells,

phloem fibers provide structural rigidity to the plant and phloem parenchyma function as storage cells for organic compounds (Evert and Eichhorn, 2006).

During plant growth, new sieve elements that lose their protoplasmic contents are sequentially added to a file of previously established sieve elements forming a continuous sieve tube (Evert and Eichhorn, 2006). The cell wall interface between these cells breaks down to form pores through which materials can pass. A structure referred to as the sieve plate remains at this interface to provide stability and docking functionality within the sieve tube member (Evert and Eichhorn, 2006). In trees, the sieve tube forms a translocating continuum stretching tens of meters long (Savage et al., 2017).

Ernst Münch first postulated that the driving force behind assimilate translocation through the sieve tube is generated by a pressure gradient existing between photosynthetic source and sink tissues (Münch, 1930). Arguments in favor of his pressure flow hypothesis remained largely conjectural for nearly a century, until advances in imaging and minimally invasive pressure measurements produced firsthand empirical support (Knoblauch et al., 2016). The hypothesis contends that as carbohydrate synthesis in source tissues increases the osmolyte concentration in sieve elements, water inflow from the xylem generates a hydrostatic pressure potential large enough to drive mass flow (Münch, 1930). Concurrently, root expansion and assimilate storage reduces the osmotic potential of sink tissue sieve elements, drawing out water and producing a lower pressure potential in the sink tissue sieve elements (Münch, 1930). This pressure difference is believed to generate the flow conditions necessary for long-distance transport of assimilates through the sieve tube (Ross-Elliott et al., 2017). An alternative model for explaining the physical basis of translocation, the high pressure manifold model, was proposed to account for the seemingly insufficient pressure gradient to drive solute flux through

the sieve tube in tall trees and the insufficient symplasmic conductance of plasmodesmata for phloem unloading (Fisher and Opalka, 1996; Fisher and Cash-Clark, 2000; Patrick, 2013). This model is characterized by high hydrostatic pressure maintenance throughout the transport phloem, with minimal pressure loss between the collection and release phloem. Instead of a large axial hydrostatic pressure differential, the rate of unloading is proposed to be regulated by high plasmodesmal conductance in the release phloem (the manifold) (Fisher and Cash-Clark, 2000; Patrick, 2013). Since its proposition, Fisher's model has gained empirical support, yet recent investigations have demonstrated that the hydrostatic pressure generated at the collection phloem is sufficient to drive translocation, in part, because sieve plate conductance is spatially modified to facilitate transport (Knoblauch et al., 2017; Ross-Elliott et al., 2017).

Mechanical damage to the plant body by herbivores is a persistent threat to phloem integrity (Knoblauch and van Bel, 1998). Two regulatory systems have been identified to sequester the effects of pressure loss in sieve tubes. P proteins are large structural proteins that are frequently observed in the sieve element periphery using transmission electron microscopy (Knoblauch and van Bel, 1998). In the event of sieve tube rupture, pressure loss displaces P proteins towards the downstream sieve plate, blocking the reverse of sap contents out of the sieve tube (Knoblauch and van Bel, 1998; Knoblauch et al., 2014). The structure of P proteins remains largely unknown, but there appears to be considerable variability across plant species (**Figure 1-1**) (Knoblauch et al., 2014). In the Fabaceae family, a type of P protein called the forisome has been found to respond to calcium signaling by growing anisotropically (Knoblauch and Peters, 2004; Knoblauch et al., 2012). Forisomes can swell in response to pressure loss, insulating the integrity of the sieve element (Peters et al., 2006). A second system in sieve tubes that regulates against pressure loss, callose deposition, is a slower and more enduring response (Radford et al.,

1998). Callose synthase catalyzes the formation of callose, a β -1,3-glucan, on sieve plants over a period of minutes (Mullendore et al., 2010). Sieve plates of *Phaseolus vulgaris* and *Cucurbita maxima* exhibit partial sieve plate pore narrowing over 60 minutes, whereas sieve plates of *Phyllostachys nuda* become completely covered with callose within 20 minutes (Mullendore et al., 2010). The role of callose deposition in flow regulation at sieve plates is likely related to its function of shaping the neck region dimensions of a pervasive pore structure found in all vascular plants: plasmodesmata (Radford et al., 1998).

Plasmodesmata

Almost every cell in the plant body shares cytoplasmic links with its neighbors in the form of plasmodesmata (Brunkard et al., 2015). These nanoscopic pores allow the passage of sugars, amino acids, ions, and hormones between cells (Brunkard et al., 2015). Plasmodesmata cross through the middle lamella and cell walls of neighboring plant cells (Evert and Eichhorn, 2006). The cell wall is a rigid matrix of cellulose embedded with pectin and hemicellulose to provide structural support for the plant and to protect the cell from rupturing due to high turgor pressure (Evert and Eichhorn, 2006). Together with the plasma membrane, the cell wall divides the plant body into two separate compartments: the symplasm, consisting of plasma membrane-bound protoplasts and plasmodesmatal interiors, and the apoplast, composed of the cell wall continuum and intercellular spaces (Evert and Eichhorn, 2006). Movement of solutes through these domains is referred to symplasmic or apoplastic transfer, respectively (Evert and Eichhorn, 2006).

Plasmodesmata are generally less than 50 nm in diameter, well below the resolving power offered by ordinary light microscopy (Bell and Oparka, 2011). Revelations about the fine

structure of plasmodesmata have historically relied on the resolution offered by transmission electron microscopy (**Figure 1-2**) (Bell and Oparka, 2011). Plasmodesmata are categorized as primary or secondary depending on their mode of formation (Evert and Eichhorn, 2006). Primary plasmodesmata are formed during cytokinesis when a cell plate partitioning daughter cells entraps a strand of endoplasmic reticulum (Evert and Eichhorn, 2006). The constricted endoplasmic reticulum, referred to as a desmotubule, is a rod-like structure that connects the networks of peripheral rough endoplasmic reticulum in neighboring cells (Evert and Eichhorn, 2006). Secondary plasmodesmata are formed *de novo* between neighboring cells through enzymatic digestion of cell wall material by pectinases, hemicellulases, and cellulases (Evert and Eichhorn, 2006). Another proposed mechanism of secondary plasmodesmatal formation suggests that half-plasmodesmata present in flanking cell walls join to form a common channel (Ehlers and Kollmann, 1996). While primary plasmodesmata are typically composed of a single, unbranched channel, secondary plasmodesmata often contain numerous branches through one or both cell walls (Evert and Eichhorn, 2006). Moreover, secondary plasmodesmata typically have a median cavity in the center of the pore structure to which branches converge (Evert and Eichhorn, 2006).

Quantification of the size exclusion limit of plasmodesmata has historically relied on dye-coupling experiments (Evert and Eichhorn, 2006). In this procedure, soluble fluorescent probes of known size are injected into a cell to test of the hydrodynamic radius will permit their entry into neighboring cells (Knoblauch et al., 2015). Small fluorescent probes, such as 27 kDa green fluorescent protein, may pass through plasmodesmata into neighboring cells, but larger fluorescent protein constructs, such as 100 kDa, may be unable to fit through the pore structure (Knoblauch et al., 2015). Establishing the size exclusion limit of plasmodesmata in cells is an

important characteristic of the symplasmic transport capacity in plants and serves as a biomechanical application of fluid hydraulics.

Fluid Mechanics in Plants

The xylem and phloem of vascular plants are biological systems that obey the laws of fluid mechanics. Like all liquids, the water and sap flowing through plant vasculature are essentially incompressible materials (Blake, 1978). Liquids, like solids, have a definite volume (Fox and McDonald, 1985). However, unlike solids, liquids flow in response to shearing forces as a result of their weaker intermolecular interactions (Bruus, 2008). When a fluid is enclosed within a vessel, such as in a sieve tube, any change in pressure is transmitted undiminished throughout the fluid and to the walls of the vessel, in accordance with Pascal's principle (Fox and McDonald, 1985). In this way, the sieve tube acts as a hydraulic system that exerts forces to drive fluid transport (Jensen et al., 2012). A hydrostatic pressure differential in the sieve tube between source and sink tissues defines the distance over which this gradient exists (Knoblauch et al., 2017).

Flow rate through a vessel is the volume of fluid per unit time that passes a cross sectional area (Fox and McDonald, 1985). The flow rate of a sieve tube is controlled by both the rate of organic compound consumption at sink tissues and its supply at source tissues (Jensen et al., 2012). Frictional forces imposed by vessel geometry and organellar contents decrease the rate of flow by increasing the time a given volume of fluid takes to be displaced (Jensen et al., 2012). Friction is one component of a more inclusive parameter referred to as resistance to flow, R , which includes all factors affecting flow rate, except pressure (Fox and McDonald, 1985). When

the effects of gravity are negligible, flow rate between any two points in a vessel of uniform cross section can be calculated as

$$Q = \frac{P_2 - P_1}{R},$$

where Q is flow rate, R is resistance to flow, and P₂ and P₁ stand for measured pressures along the vessel (Fox and McDonald, 1985). High fluid viscosity and increased vessel length decrease flow rate by increasing flow resistance. Inversely, a large pressure difference across a vessel and a wider vessel diameter elevate flow rate.

Two types of internal flow exist: laminar flow and turbulent flow (Fox and McDonald, 1985). Fluids which flow smoothly in layers (lamina) that do not mix exhibit laminar flow (Fox and McDonald, 1985). Those which are characterized by heavy mixing due to eddies and swirls demonstrate turbulent flow. This dichotomy is useful for understanding the two different flow regimes, but internal flows in most biological systems are a blend of both flow types (LaBarbera, 1990). Laminar flow predominates in small vessels with viscous fluids, such as in sieve elements and plasmodesmata (Blake, 1977; Blake, 1978). Poiseuille's law of resistance describes the impact of flow resistance-relevant parameters in laminar flow systems and is stated as

$$R = \frac{8\eta l}{\pi r^4},$$

where R is resistance to flow, η is fluid viscosity, l is the length of a vessel, and r is the vessel's radius (Bruus, 2008). Both viscosity and vessel length are directly proportional to laminar flow resistance. For example, doubling the viscosity of a fluid or vessel length through which a fluid travels increases flow resistance by a factor of 2. A more dramatic consequence on flow resistance is observed by changing the radius of a vessel – doubling this parameter decreases flow resistance by a factor of 16. Consequently, minor changes to the diameter of a plant vessel

have a considerable impact on the efficiency with which the organism can transport materials through the vasculature (Mullendore et al., 2010).

Phloem Unloading in the roots of *Arabidopsis thaliana*

Prior to their circulation to the rest of the plant body, sugars in source tissues must transfer into the vasculature, typically through the minor veins of leaves, by a process called phloem loading (Rennie and Turgeon, 2009). Plant species employ one of several possible pathways to accomplish this loading process (**Figure 1-4**) (Rennie and Turgeon, 2009). In passive loading, the hydrostatic pressure generated by sucrose production in source tissues is large enough to drive assimilate flow into plasmodesmata of the SECCC and through the transport phloem to the release phloem, where it is consumed by metabolic activity or storage (Rennie and Turgeon, 2009). A variation of passive loading includes a mechanism of polymer trapping, where sucrose that is transported into the SECCC becomes sequestered due to the smaller apertures of concentrated plasmodesmata and assimilation of sucrose molecules into larger carbohydrates, raffinose and stachyose (Rennie and Turgeon, 2009). An alternative loading strategy, apoplastic loading, involves active transport of sucrose molecules from the apoplasm into the symplasm of the SECCC by sucrose transporters (SUCs or SUTs) (Baker et al., 2016). Vascular plants that employ this strategy often have smaller axial pressure gradients and lower concentrations of transport compounds (Rennie and Turgeon, 2009).

Symplasmic unloading of assimilates from the release phloem SECCC into the post-phloem domain is a common pathway in all plant roots, although certain sink structures require an obligate apoplastic step (Patrick, 2013). The tissue organization and cellular ultrastructure define the pathway and hydrodynamics in which assimilates are unloaded (Patrick, 2013).

Further, the dimensions of the cell wall interfaces surrounding sieve elements and the total cross-sectional area forming symplasmic connections to neighboring cells are rate-limiting considerations (Patrick, 2013). Hydraulic conductance regulates symplasmic unloading in release phloem rather than a hydrostatic pressure differential, consistent with the high pressure manifold model (Patrick, 2013; Ross-Elliott et al., 2017). This feature of phloem unloading through plasmodesmata is pertinent in establishing the characteristics of flow into the post phloem domain of roots (Ross-Elliott et al., 2017). The discovery of a type of plasmodesma in *Arabidopsis thaliana* that reflects a funnel shape advanced this theory because the configuration of the structure allows conduction through the plasmodesma to be twenty times as efficient (Ross-Elliott et al., 2017). Funnel plasmodesmata exist in the cell walls between protophloem sieve elements, the transitory sieve elements through which phloem payloads are delivered, and phloem pole pericycle cells, into which assimilates are unloaded (**Figure 1-5**) (Ross-Elliott et al., 2017). The organization of cells around protophloem sieve elements in the unloading zone of *A. thaliana* appears to be conserved (**Figure 1-6**), with two peripheral phloem pole pericycle cells, two lateral companion cells, and one immature metaphloem sieve element towards the center of the vascular cylinder which opens up and carries out phloem conduction later in development (Ross-Elliott et al., 2017). The details of hydraulic flux through funnel plasmodesmata and the organization of protophloem in the roots of other species are promising areas of research to elucidate the unloading process.

Preservation of Plant Tissue

In order to make valid and accurate judgements about plant tissue structure, a reasonable number of measures must be carried out to closely imitate the true living state of a sample.

Probing a biological specimen invariably disrupts the stable equilibrium in which the specimen is programmed to operate. An effective preparation protocol must stringently preserve cellular ultrastructure and simultaneously protect the fine microanatomy of membranes and macromolecular particles. If a tissue of interest is located deep within a specimen, a series of incremental chemical infusions must be carried out to stabilize the target prior to mechanical extraction (Bozzola and Russell, 1998). The workflow for preparing samples for analysis is determined by the type of data which one seeks to attain. Obtaining images that are of sufficient quality for measurements and inference is contingent on each step of the sample preservation protocol being implemented properly.

Figure 1-3 illustrates the main steps involved in sample preparation for a biological specimen whose fine structure is to be imaged by transmission electron microscopy. A fresh, hydrated plant specimen is first chemically fixed using aldehydes such as paraformaldehyde, glutaraldehyde, or a combination of the two to utilize both paraformaldehyde's faster infusion rate and glutaraldehyde's greater crosslinking ability (Bozzola and Russell, 1998). The concentration of fixative penetration into a tissue reduces considerably over a short distance, so cutting samples into cubic volumes of about 1 mm in each dimension facilitates aldehyde infusion (Daniel Mullendore, personal communication, August 1, 2016). Immersing samples in a buffered solution that reflects a pH of 7.2, such as phosphate buffer, cacodylate buffer, or piperazine-N,N'-bis(2-ethanesulfonic acid) (PIPES) buffer, inhibits potentially detrimental effects on tissue structure resulting from pH shifts (Bozzola and Russell, 1998). Infiltration of these chemicals may also be assisted by subjecting the immersed sample to microwave irradiation or elevated pressure (Bozzola and Russell, 1998).

Aldehydes effectively bind proteins, but are less efficient at binding lipids, carbohydrates, and nucleic acids (Bozzola and Russell, 1998). After thoroughly washing off primary fixatives, osmium tetroxide is routinely applied to secure lipids and biological membranes during a process referred to as post-fixation (Porter and Kallman, 1952; Bozzola and Russell, 1998). The osmium tetroxide molecule consists of four oxygen atoms bound to a central osmium atom by double bonds (Porter and Kallman, 1952). Osmium tetroxide oxidizes the unsaturated bonds of hydrocarbon chains in lipids, creating crosslinked networks (Porter and Kallman, 1952; Bozzola and Russell, 1998). Osmium tetroxide stains biological samples with a distinguishing black tinge and improves contrast under an electron microscope (Porter and Kallman, 1952; Bozzola and Russell, 1998).

After washing off osmium tetroxide, water must be removed from the sample (Bozzola and Russell, 1998). This task is usually achieved by serial dehydration, during which gradually increasing concentrations of an organic solvent like ethanol, methanol, or acetone replace water in the specimen (Bozzola and Russell, 1998). Whereas animal and most bacterial cells are relatively pervious to solvent infiltration, plant cells demand more rigorous infusion due to their cell walls built of dense network of cellulose. Integrating more dehydration steps, waiting longer in between solvent replacement, and assisting solvent infiltration by microwave irradiation are potential strategies to increase the efficiency of dehydration (Bozzola and Russell, 1998).

The purpose of resin embedding is to enmesh a biological specimen in a curable material that can be cut into sections to expose cell fractions for visualization (Bozzola and Russell, 1998). A variety of resins have been developed for this purpose, being derived both naturally from trees and artificially from organic synthesis (Bozzola and Russell, 1998). Common resin products with unique physical and histochemical properties include epoxy resin 812, araldite,

Spurr's resin, and LR White (Bozzola and Russell, 1998). Plant cells are fairly impermeable to most resin monomers, so a highly miscible adjuvant like propylene oxide is used as a transition solvent to facilitate resin entry(Bozzola and Russell, 1998). Subjecting a sample through a graded series of resin solutions elevates the internal resin concentration in cells (Bozzola and Russell, 1998). After several days of incubation in 100% resin on a stirring platform, the embedded samples can be cured (hardened) in an oven to form a block for sectioning (Bozzola and Russell, 1998).

The process of sectioning is carried out in a microtome, which is a precision instrument for cutting mounted samples against a knife edge made of glass, steel, or diamond (Bozzola and Russell, 1998). This stage of the preparation workflow for imaging serves the dual purpose of producing thin sections for fine structure illumination by the electron microscope and permitting thick section collection to survey tissue fixation quality by light microscopy (Bozzola and Russell, 1998). In practice, thin sections should be between 50 and 100 nm in diameter for the electron beam to penetrate the specimen and provide superior resolution (Bozzola and Russell, 1998). Thick sections typically vary between 0.5 and 2.0 μm , but these values can vary widely depending on the purpose of thick section acquisition (Bozzola and Russell, 1998). Thick sections may be obtained to confirm that a specimen is ready for thin sectioning or may be used for data collection themselves (Bozzola and Russell, 1998). A plethora of chromatic dye options exist to differentiate between tissues based on their chemical profiles. For plant tissues, toluidine blue, Fuchsin-Chrysoidin-Astrablue (FCA), aniline blue, Sudan IV, calcofluor white, and phloroglucinol are routinely used to label tissues and increase sample contrast (Bozzola and Russell, 1998). For thin sections, contrast enhancement is achieved, in part, by adding heavy metals to section surfaces. The abundance of secondary electrons in the outer orbitals of these

elements improve signal detection by the charge-coupled device (CCD) camera. Uranyl acetate and Reynold's Lead are staining standards for electron microscopy (Bozzola and Russell, 1998). Better resolution of the membranous components of plant cells may be achieved by applying tannic acid and potassium permanganate either at this stage of staining or earlier during fixation (Bozzola and Russell, 1998).

Imaging Plants

A variety of sophisticated imaging instruments have been developed to acquire data from microscopic samples. High quality compound light microscopes are capable of magnifying objects by hundreds of times their actual size (Evert and Eichhorn, 2006). By focusing light that is refracted through a series of glass lenses, both embedded and living tissues can be viewed in detail. Contemporary light microscopes often include a built-in camera for electronic image collection. Image acquisition with the aid of an optical device capable of digital processing permits greater control over the color space and quality aspects of image formation. Many compound light microscopes also offer functionality for fluorescence experiments. Fluorescence refers to the observed emission of lower energy light by a material that absorbs light of shorter, higher energy wavelengths (Evert and Eichhorn, 2006). By applying fluorophores that bind specifically to sub-optical structures in a specimen, fluorescence microscopy is capable of producing image overlays that map multiple biological targets simultaneously (Knoblauch et al., 2015).

Higher resolution imaging is achieved through confocal laser scanning microscopy (LSCM), which incorporates two pinholes that block out-of-focus light to produce clearer images (Carlsson, 1985). This technique of imaging permits deeper exploration at high resolution by

optically sectioning into a specimen (Carlsson, 1985). By combining or flattening tandem optical sections, 3D or compressed 2D representations of living systems may be obtained (Carlsson, 1985). LSCM can process a larger number of labeled targets with the help of high precision lasers and numerous detectors (Knoblauch et al., 2015). Furthermore, this platform is useful for investigating physiological process in real time, such as phloem unloading in roots (Oparka et al., 1994). A new generation of super-resolution microscopes designed to meet, or artificially surpass, the optical constraints imposed by the diffraction limit of light improve upon the design of confocal microscopes to enable techniques like photon tunneling and single-molecule localization (Schermelleh et al., 2010).

While photons are useful for probing living cells and collecting signals several layers deep into tissue, the light diffraction limit of 200 nm prevents the resolution of structures like ribosomes and plasmodesmata. An alternative particle that can be used to illuminate samples is the electron, which has a far shorter wavelength of 2.5 pm at 200 keV. The electron microscope directs a beam of accelerated electrons into a small sample to produce high resolution images. Two types of electron microscopes are widely used today: scanning electron microscopes and transmission electron microscopes. The scanning electron microscope resolves surface topological features from a 3D perspective. After clearing sieve elements of their protoplasmic contents, Mullendore et al. (2010) used scanning electron microscopy to image the interiors of these cells. After extracting geometrical information from the cell walls and sieve plates, they were able to characterize the conductivity of sieve tubes and the effects of callose deposition on flow. Similar to scanning electron microscopes, transmission electron microscopes provide nanoscale resolution, require sample immobilization, and operate under a vacuum, necessitating complete sample dehydration (Bozzola and Russell, 1998). Transmission electron microscopes

produce detailed 2D images of cellular fine structure (Bell and Oparka, 2010). Froelich et al. (2011) presented evidence of P proteins organizing into stacks in transmission electron micrographs while contending that P protein agglomerations do not affect translocation. Modern TEMs are equipped with technology which rotates sample holders so a stacks of images can be produced and reconstructed into 3D volumes in a process called electron tomography (Daum and Kühlbrandt, 2011). This method can be used to extract highly-resolved, information-rich images from sections and be converted into structural models for further experimentation, such as flow analysis (Tariq et al., 2011; Stanfield et al., 2018).

My Research

In chapter 2, we describe the root protophloem unloading network in a collection of angiosperm species. Our first aim was to develop a tissue preservation procedure that stringently captures the fine ultrastructural details of plant cells necessary to model flow dynamics. Microwave irradiation and supplemental post-fixation with OsO₄ enhanced fixation conditions for most species. We provide images of root cross sections from the unloading zone of each species to exhibit fixation quality. Most protophloem files exhibited a similar cellular architecture to *Arabidopsis thaliana*, yet *Triticum aestivum*, *Oryza sativa*, and *Solanostemon scutellarioides* protophloem files contained four vascular parenchyma neighbors rather than five. Transmission electron micrographs of plasmodesmata are offered to demonstrate their morphological variations in the root protophloem. We compare several funnel plasmodesmata geometrical measurements in different species and propose a conceptual model for predicting true aperture diameters from two-dimensional images. Performing electron tomography on plasmodesmata enabled us to reconstruct full structural volumes. Analyzing a funnel

plasmodesma from *T. aestivum* by the finite element method allowed us to model laminar flow through a plasmodesma for the first time. While outlet flow velocity was on the order of 0.05 m/s, inlet flow was less than 0.015 m/s on average. Our research throws light on the structural diversity in root protophloem and describes a workflow for visualizing and performing experiments on plasmodesmata in a new way.

Figures

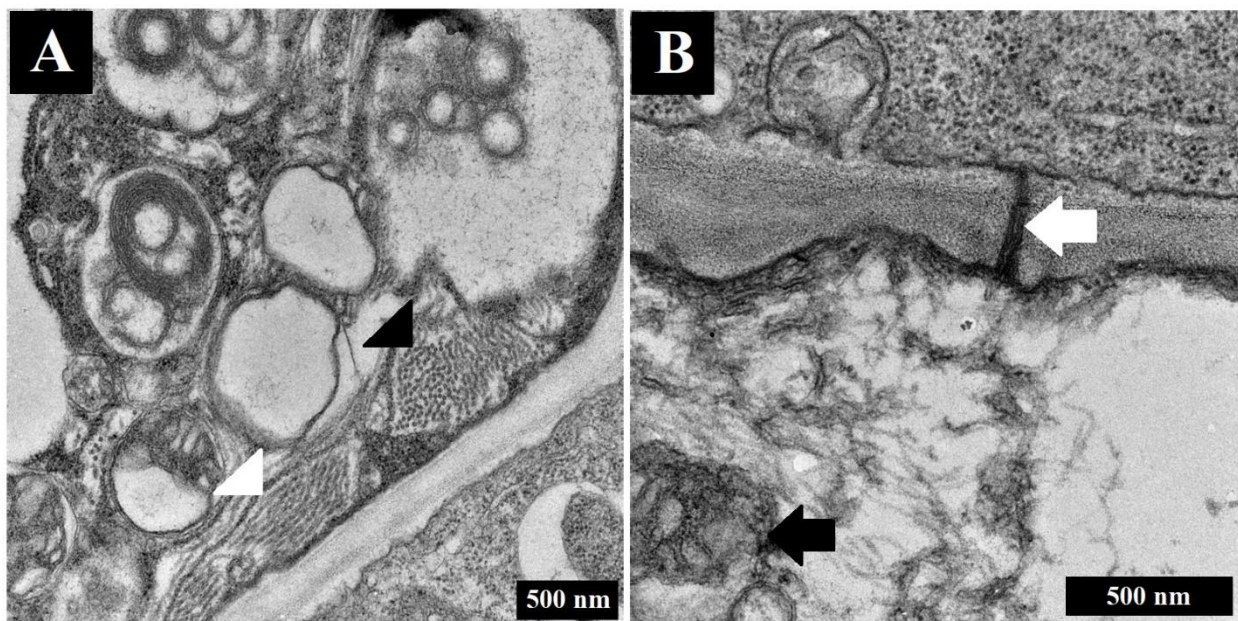


Figure 1-1 Subcellular features of sieve elements. (A) A cell wall divides a sieve element (top-left) and a companion cell (bottom-right) in *Ipomoea nil*. Bundles of filamentous P proteins are observed in cross section (black arrowhead) and longitudinal/oblique section (white arrowhead). (B) Filamentous P proteins are scattered in the sieve element lumen of *Medicago sativa* around one type of organelle found in mature sieve elements, a mitochondrion (black arrow). The cell wall separating a sieve element from its neighboring cell encases a plasmodesma (white arrow) which facilitates intercellular communication.

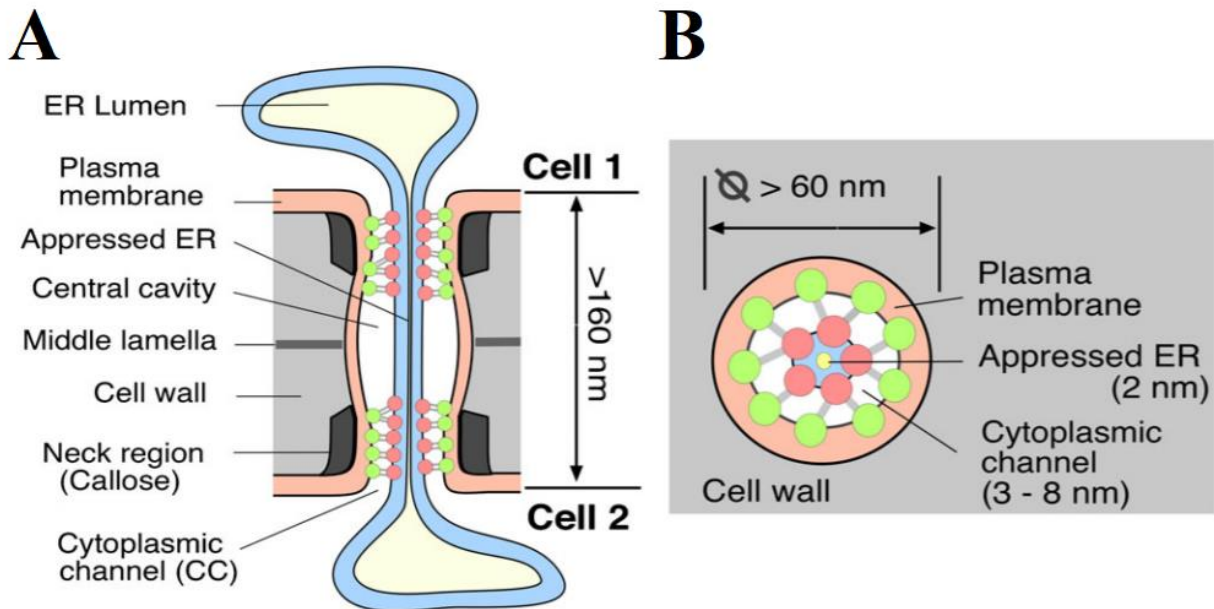


Figure 1-2. A schematic representation of the components present in a typical plasmodesma. (A) Longitudinal view of a plasmodesma exhibiting a single continuous system of endoplasmic reticulum (ER, beige compartment encased in a blue-labeled membrane) traversing the cell wall (gray). (B) A cross sectional view of the desmotubule encased within the plasmodesma demonstrates that the appressed ER it stabilized within the plasmodesma by a system of spokes (fuchsia-green dumbbells) anchored to the plasma membrane (tan), forming a cytoplasmic sleeve (white) through which nanoscopic cellular contents may pass into the neighboring cells. This is a modified figure from Lucas et al. (2001) that was obtained from Kragler (2013).

SAMPLE PREPARATION FOR IMAGING

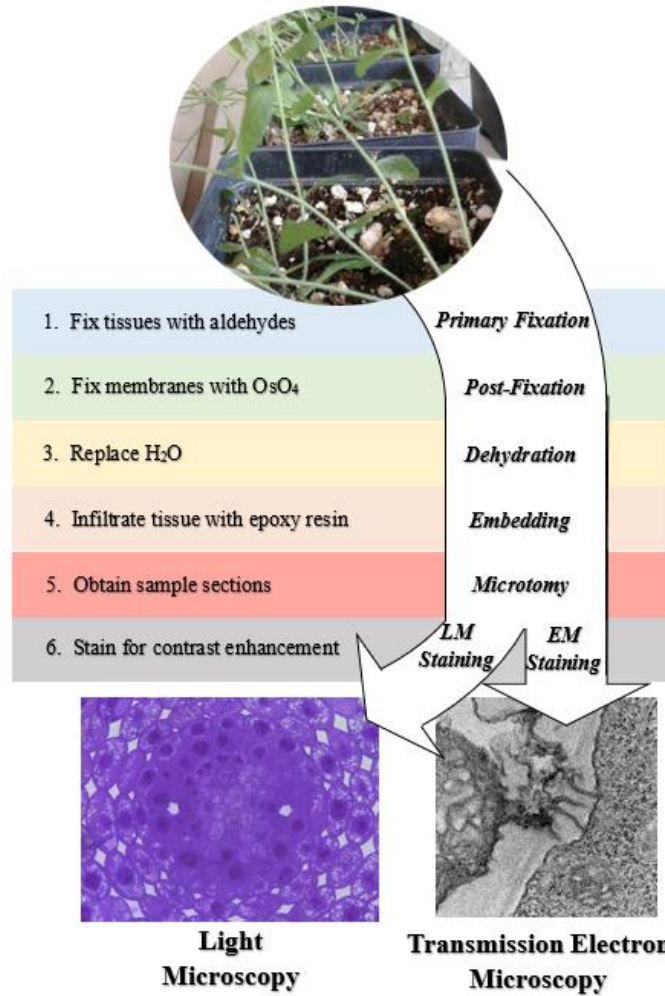


Figure 1-3 Workflow for preparing biological samples for imaging by light and electron microscopy. Here, plant tissue is fixed, dehydrated, embedded, sectioned, stained, and imaged to produce micrographs of root tissue.

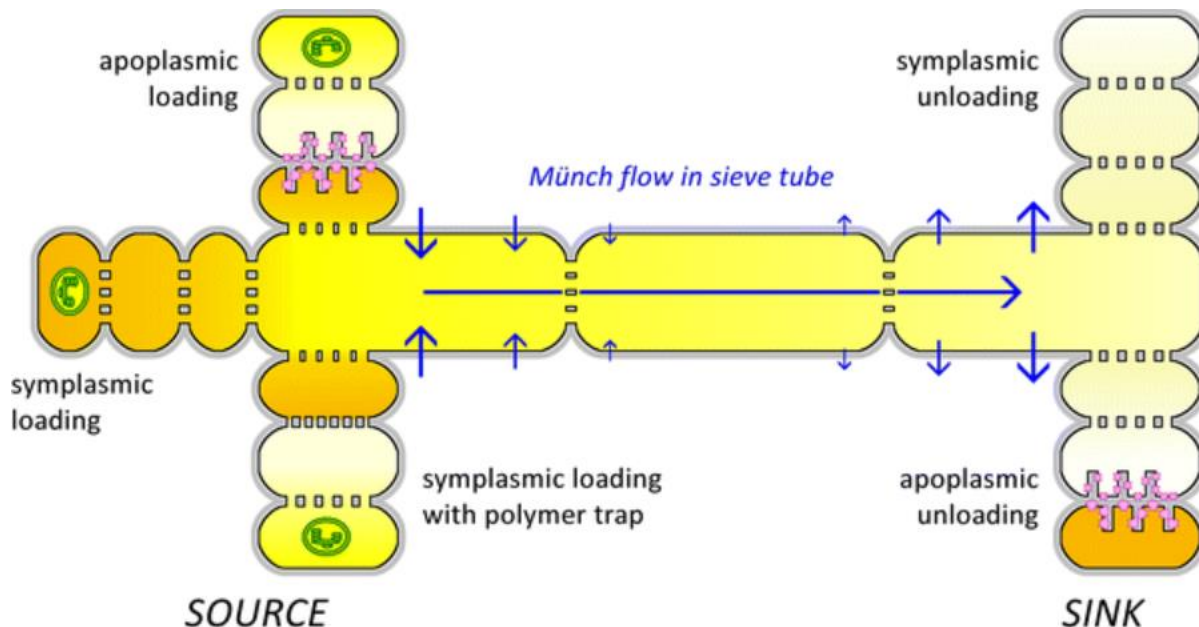


Figure 1-4. A schematic diagram of phloem-mediated assimilate transport pathways. The left side of this diagram describes mechanisms of assimilate phloem loading from source tissues. Sugars produced during photosynthesis transfer into the sieve tube by either apoplastic loading, which utilizes active transport (transport proteins, pink dots) to import sugars into the SECCC, or by symplasmic transport, where sugars travel down a concentration gradient (orange-yellow transition) through mass flow by way of plasmodesmata. A variant of symplasmic loading involves polymer trapping, the synthesis of larger carbohydrates from sucrose substrates, which are unable to move back through narrow plasmodesmata separating the SECCC. Water flux is represented by blue arrows. The vascular payload follows the long blue arrow to sink tissues, where assimilates are unloaded symplasmically or apoplasmically. This illustration incorporates all identified loading and unloading mechanisms into one model for didactic purposes only. This figure was obtained from Knoblauch and Peters (2013).

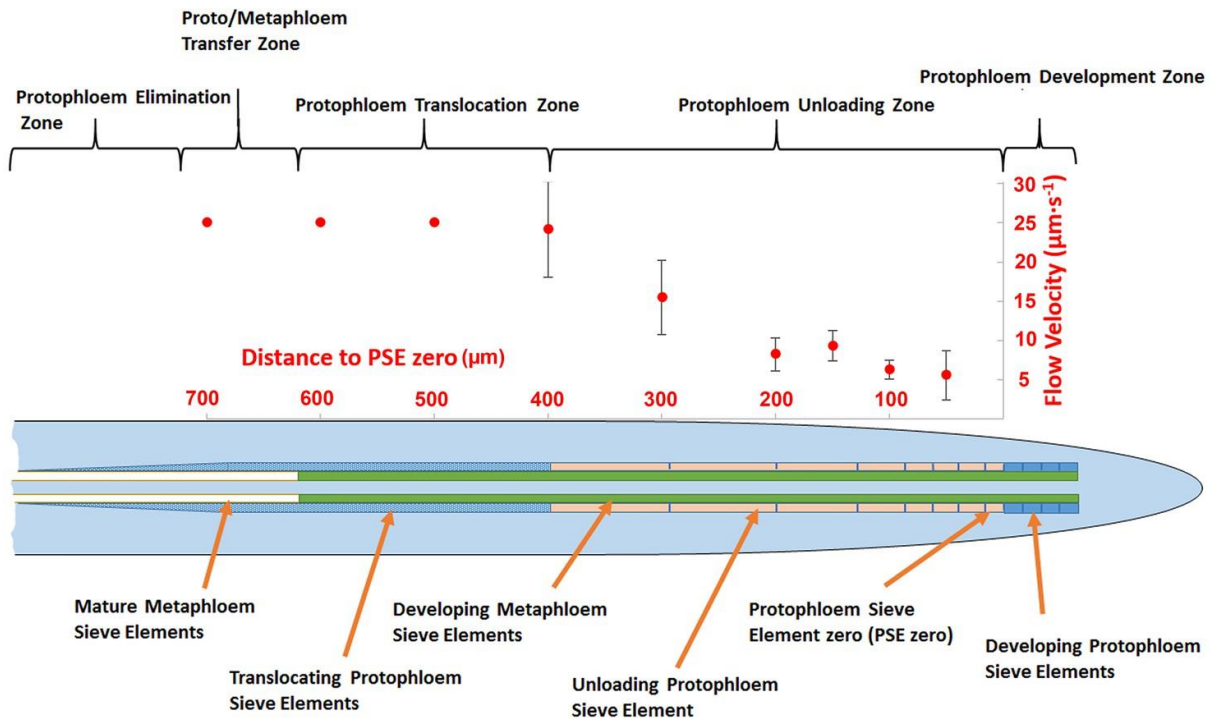


Figure 1-5. A schematic diagram of functional regions related to phloem elongation and assimilate unloading in *Arabidopsis thaliana* roots. During root growth, protophloem initials differentiate and lose most of their cytoplasmic contents before being added to the sieve tube. The protophloem cell next in line to be added to the sieve tube is referred to as protophloem sieve element zero. Experimentally-derived flow velocity measurements along the sieve tube are posted above the root to illuminate the connection between assimilate movement and the structural domain of the unloading zone (beige). This figure was obtained from Ross-Elliott et al. (2017).

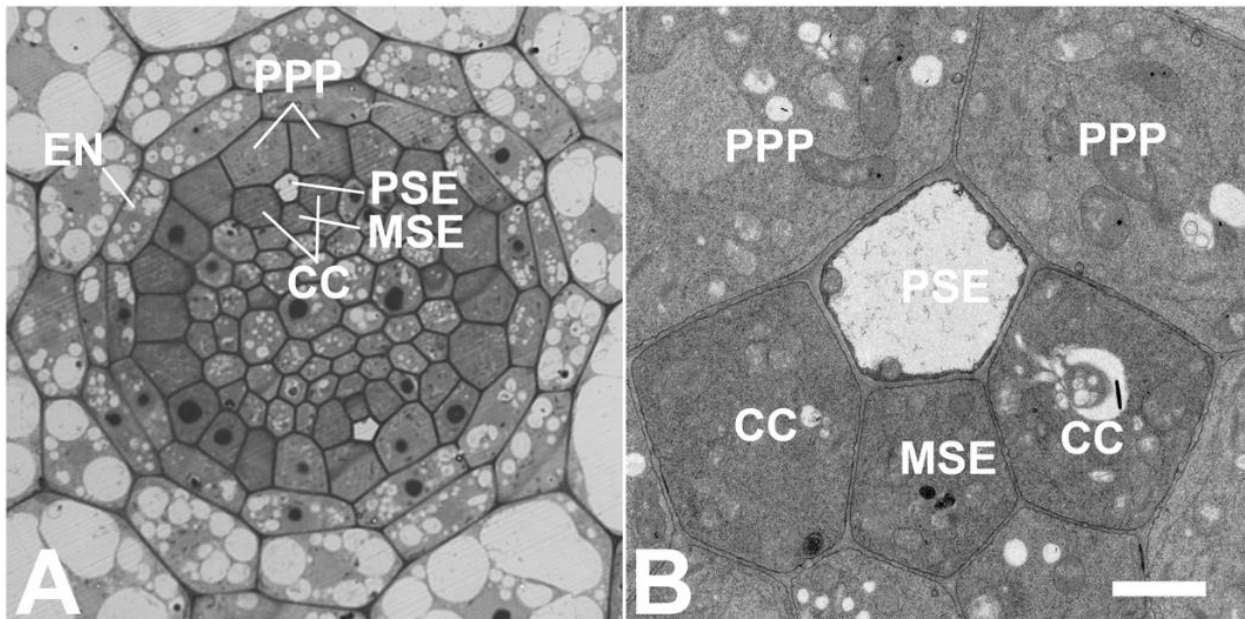


Figure 1-6. Ultrastructural organization of vasculature observed in cross section through the root unloading zone of *Arabidopsis thaliana*. (A) Two functional protophloem files are present in the central cylinder. (B) Delivery of phloem contents is mediated by the PSE. In *A. thaliana*, the most frequently observed neighbors of the PSE are two peripheral PPP cells, two lateral CC, and one central MSE cell. PSE, protophloem sieve element; PPP, phloem pole pericycle; CC, companion cell; MSE, metaphloem sieve element. Bar: 5 μm . This figure was obtained from Ross-Elliott et al. (2017).

CHAPTER TWO: MODELING THE STRUCTURE AND FLOW DYNAMICS OF
PLASMODESMATA FROM THE UNLOADING ZONE OF
ANGIOSPERM ROOTS

By

Grayson P. Ostermeyer¹, Winfried S. Peters¹, Aslak R. Franzen^{2*}, Kaare H. Jensen^{2*}, and
Michael Knoblauch¹

¹ School of Biological Sciences, Washington State University, Pullman, WA 99164

² Department of Physics, Technical University of Denmark, Kongens Lyngby, Denmark

¹ This study was supported by a grant from the National Science Foundation (award IOS 1146500).

* Corresponding authors

Abstract

Vascular plants use the phloem to transport photoassimilates to sink tissues, driving important processes such as root growth and nutrient storage. The design of the root unloading zone regulates discharge capacity into the post-phloem domain and is organized at both the cellular and ultrastructural levels. Unloading of phloem contents occurs through sub-microscopic pores called plasmodesmata, which exhibit intricate morphological and distributive patterns. We begin by illuminating the anatomical features of protophloem in a collection of angiosperm roots. With the aid of electron tomography, we generated 3D reconstructions of distinct plasmodesmata varieties from the unloading zone. Flow characteristics of a *T. aestivum* funnel plasmodesma are demonstrated by finite element analysis. These experiments exhibit the effects of fine structure on flow efficiency through plasmodesmata. Altogether, we demonstrate the value of an innovative approach for visualizing, measuring, and modeling flow through plasmodesmata, which present a new platform for engineering more productive crops.

Introduction

A key mechanism contributing to the evolutionary success of vascular plants is the ability to redistribute the products of photosynthesis to tissues that specialize in other physiological tasks. Channeling photoassimilates through the phloem vasculature is a functionally efficient technique for nutrient transport, both in terms of delivery time and the quantity of assimilates displaced, because the flux rate of bulk flow through a laminar system far exceeds that of simple diffusion (Dölger et al., 2014). Chains of interconnected sieve tube elements in the phloem form the vessels that facilitate the process of assimilate conduction. Carbohydrate-rich payloads sourced from aerial organs pass through the transport phloem to supply fuel for the metabolic activities of distant sink organs, such as the subterranean roots (Knoblauch and Peters, 2013). The capacity for photosynthate allocation into sink tissues serves as a basis of agricultural productivity, as increased plant investment into storage organs like grains and tubers translates into larger crop yields (Savary et al, 2012).

Details about the processes driving assimilate transport through the phloem have lagged behind other realms of plant biophysics because phloem conduction, understood at the organismal level, is regulated by the intricate, microscopic fine structure of the assimilate transport pathway (Knoblauch and Peters, 2013). Nevertheless, several propositions have been offered to explain the process of phloem-mediated transport in vascular plants. Ernst Münch relied on first principles to justify his pressure flow hypothesis, the first unified proposition about long-distance transport published in 1930 (Münch, 1930). According to the Münch hypothesis, a pressure gradient generated between photosynthetic source and sink tissues drives bulk flow of assimilates throughout the plant body. Passage of assimilates into the sieve tube at the collection phloem elevates the local osmotic potential, driving xylem-sourced water into the tube and

thereby increasing its local hydrostatic pressure (Münch, 1930). In the growing root, assimilates are expended to catalyze endergonic biochemical reactions, reducing local osmotic potential and alleviating local hydrostatic pressure by water leakage (Münch, 1930). The disparity in hydrostatic pressure between sieve tube terminals provides the driving force for flow to occur along the source-path-sink system (Münch, 1930). A physical intuitiveness about the pressure flow hypothesis may have played a role in its tenacity, but the lack of empirical evidence in support of its practicality left many uncertain of the model's accuracy (Patrick, 2013). A key area of contention that surrounded the pressure flow hypothesis was whether the magnitudes of axial hydrostatic pressure gradients were sufficient to drive flow through long sieve tubes, especially in those of tall trees (Patrick, 2013). In an alternative hypothesis, Donald Fisher contended that a gradient of hydrostatic pressure along the sieve tube was unlikely to exist (Fisher and Cash-Clark, 2000). Rather, he argued that incremental changes to the hydrostatic pressure in sieve tubes by osmolyte loading would be quickly dissipated, and that negligible difference in hydrostatic pressure exists along the sieve tube (Fisher and Cash-Clark, 2000). High hydrostatic pressure is postulated to be maintained, in part, by axial paths of low hydraulic conductance provided by transfer phloem plasmodesmata and retrieval of leaked sucrose by sucrose importers (SUTs) (Patrick, 2013). Unloading of assimilates, according to the high pressure manifold hypothesis, is facilitated by the hydraulic conductance of plasmodesmata in the release phloem, rather than by axial hydrostatic pressure (Patrick, 2013). The divide between both models was addressed by Knoblauch et al. (2016) in an investigation that utilized micro-capillary pressure probes and imaging platforms to quantify sieve tube flow characteristics in the vine, *Ipomoea nil* (Knoblauch et al., 2016). They found that flow-relevant parameter measurements scaled in elongated vines, pruned of their axial leaves, as predicted by the Hagan-Poiseuille of hydraulic

resistance (Knoblauch et al., 2016). This result was attributed the 5-to-6 fold increase in sieve tube conductance gained by increased average sieve plate pore radii compared to a fully foliated vine (Knoblauch et al., 2016). This result reconciled one disparity between the pressure flow and high-pressure manifold hypotheses, yet resolving the structure and dynamics involved in phloem unloading would shed more light on the accuracy of these assimilate translocation models.

Phloem unloading is the process of transporting phloem-mobile compounds that have been translocated to release phloem to sites of metabolism and/or compartmentation (Patrick, 1997). The sequence of transport events through which assimilates are channeled during phloem discharge defines the pathway of phloem unloading (Patrick, 1997). Vascular plants share a common symplasmic mechanism of phloem unloading, however, specialized conditions that require assimilate partitioning into the apoplasm follow an apoplastic mechanism, such as in the axial pathway in plants with a low source/sink ratio and the unloading pathway for developing seeds (Patrick, 1997). Both unloading flux and the cross-sectional area through which assimilates travel are limiting factors in the symplasmic unloading pathway (Patrick, 1997). In roots, phloem unloading is carried out through a transient subapical tissue known as the protophloem (Patrick, 1997). Symplasmic unloading out of protophloem sieve elements is regulated by neighboring cell wall dimensions and the hydraulic conductivity of plasmodesmata connecting cells across those interfaces (Patrick, 1997). Resolving the cellular pathway through which assimilates pass from sieve elements to recipient sink cells is a central aim in understanding root unloading dynamics, however, knowledge about protophloem ultrastructure has trailed that of other plant domains because it is situated beneath several obscuring layers of cortex and loses its delicate configuration in response to mechanical damage or excision (Patrick, 1997).

Ross-Elliott et al. (2017) provided a highly detailed account of the ultrastructure of the model plant *Arabidopsis thaliana*, as well as the root unloading dynamics of this species, using a combination non-invasive imaging, 3D electron microscopy, and mathematical modeling. They found a conserved pattern of five cellular neighbors around root protophloem sieve elements in the root unloading zone that together act as a filtration system for symplasmic unloading (Ross-Elliott et al., 2017). Both files of protophloem sieve elements are adjacent to an immature metaphloem sieve element towards the center of the vascular cylinder, a type of sieve element that loses much of its protoplasmic contents when the cell joins the conducting vessel of mature metaphloem later in development (Ross-Elliott et al., 2017). Two lateral companion cells were observed adjacent to each protophloem sieve element which provide metabolic support to the sieve element (Ross-Elliott et al., 2017). Two phloem pole pericycle cells joined the protophloem sieve elements at their peripheral interface. Ross-Elliott et al. (2017) demonstrated through elegant dye-coupling experiments that the phloem pole pericycle acts as a repository for unloaded macromolecules and that a batch unloading mechanism differentially unloads phloem-mobile payloads by size (Ross-Elliott et al., 2017). A novel type of plasmodesma, a funnel plasmodesma, was discovered along the protophloem sieve element-phloem pole pericycle interface in *A. thaliana*. Ross-Elliott et al. (2017) proposed a link between the unique dimensions of this plasmodesma type with the phloem sap flux directed into the phloem pole pericycle. Using serial block face scanning electron microscopy, the group acquired three dimensional of the root protophloem in *A. thaliana*, including plasmodesmata types at each interface and their relative abundances (Ross-Elliott et al., 2017). Funnel plasmodesmata were found only at the phloem pole pericycle cell interface, whereas branched plasmodesmata populated the companion cell interface and simple plasmodesmata were most common at the metaphloem sieve element

interface (Ross-Elliott et al., 2017). Evaluating structural and functional data under several unloading pattern scenarios, Ross-Elliott et al. (2017) determined that bulk flow dominates during root phloem unloading in *A. thaliana*, while unloading by diffusion contributes little to symplasmic unloading. The proposed model of convective phloem unloading reflects the dominant unloading mechanism in *A. thaliana* roots, the first species to have its symplasmic unloading network described in detail (Ross-Elliott et al., 2017).

Here, we expand on the work of Ross-Elliott et al. (2017) to shed light on the variations in root protophloem ultrastructure exhibited in a collection of angiosperm species. Our analysis highlights the diversity in protophloem ultrastructure to demonstrate the cellular pathways present for assimilate unloading. We provide examples of frequently observed plasmodesmata types observed in the cell walls between protophloem sieve elements and their neighbors to provide evidence of symplasmic channels that assimilate flow through. We then explore the geometry of funnel plasmodesmata through manual measurement and mathematical modeling. To extract full funnel plasmodesma volumes, we utilize 3D electron tomography. Using one of the reconstructions, we describe the hydraulic characteristics of simulated laminar flow.

Results

Divergent Protophloem Anatomy in Plant Roots

We chose to investigate the architectural variations exhibited by root protophloem in a collection of diverse angiosperm plants to first illuminate how they deviate from *Arabidopsis thaliana*. Each plant belongs to one of the three identified phloem loading types – apoplasmic, passive, or polymer trapping (Rennie and Turgeon, 2009). *Triticum aestivum* (spring wheat) and *Oryza sativa* (Asian rice) are valuable agricultural commodities (Haile, 2016) and common crops

in contemporary plant research (Evers et al., 2005; Goff et al., 2002). Both *T. aestivum* and *O. sativa* belong to the Poacea family of the monocot lineage (Bessey, 1915). *Nicotiana tabacum* (tobacco) belongs to the Solanaceae family and loads apoplasmically (Bessey, 1915; Rennie and Turgeon, 2009). This eudicot is a useful model organism in plant physiology research because it grows quickly and is amenable to tissue culture and genetic engineering (Ganapathi et al., 2004). *Ipomoea nil* (morning glory) is a vine from the Convolvulaceae family that likely loads apoplasmically (Bessey, 1915). The indeterminate growth strategy of this species rendered it useful for assessing the biomechanics of transporting assimilates through the phloem over long distances (Knoblauch et al., 2017). *Medicago sativa* (alfalfa) is a cash crop of the family Fabaceae that loads apoplasmically (Bessey, 1915; Zhang et al., 2014). *Solenostemon scutellarioides* (*Coleus blumei*, painted nettle) is an ornamental plant that uses a polymer trapping strategy of phloem loading and belongs to the Lamiaceae family (Rennie and Turgeon, 2009). *Catalpa speciosa* (northern catalpa) is a tree that also loads assimilates through polymer trapping (Rennie and Turgeon, 2009). This species belongs to the Bignoniaceae family (Bessey, 1915). We included *Quercus rubra* (red oak), a tree from the Fagaceae family, in our investigation to study the root microanatomy of a passive loading species (Bessey, 1915, Rennie and Turgeon, 2009).

Having evolved over millions of years in diverse environments since divergence, each species has adopted distinct biochemistries to which preservation protocols had to be tailored (de Neergaard et al., 2000; Bais et al., 2001). Fortunately, routine preparation techniques for electron microscopy are robust for most biological specimens, so only minor alterations were integrated into our imaging workflow. Microwave-assisted primary fixation of excised root tips in 0.05 M cacodylate-buffered solutions of 2% paraformaldehyde and 2% glutaraldehyde effectively

preserved cytoplasmic contents in all species and limited osmotic-induced artifacts such as plasmolysis. While subjecting tissues to high concentrations of fixative can cause denaturation, using too low fixative concentrations risks incomplete sample preservation (Bozzola and Russell, 1998). Our solution was designed to balance the high penetrance of paraformaldehyde with the higher cross-linking ability of glutaraldehyde suited to plant roots (Bozzola and Russel, 1998). We subjected the samples to microwave irradiation at 750 W for two 90-second sessions, allowing heat to dissipate for one minute in between sessions. A cooling system prevented sample temperatures from rising above 35 °C. Samples fixed in PIPES and phosphate buffer, and those fixed in 0.2 M and 0.1 M cacodylate buffer, exhibited higher plasmolysis, an osmotic artifact, compared to 0.05 M cacodylate buffer. After rinsing several times in ddH₂O, we post-fixed samples in a 1% OsO₄ solution overnight at 4 °C. This secondary fixation regime was sufficient for *N. tabacum* and *S. scutellarioides*, however, the other species demanded additional incubation in OsO₄ for adequate fixation. *I. nil*, *M. sativa*, and *C. speciosa* root fixation quality improved after being subjected to 2% OsO₄ treatment for approximately 30 minutes at room temperature (23 °C). Two hours of additional post-fixation in 2% OsO₄ markedly improved the preservation quality of *T. aestivum* and *O. sativa*. Larger root diameter and greater lignification in monocot roots may have structurally hindered OsO₄ infusion (Schreiber et al., 1999). After several rinses with ddH₂O, we subjected the samples to a microwave-assisted methanol dehydration series consisting of 10% incremental steps. We chose methanol because it was shown to preserve tissue size and morphology better than other organic solvents, such as acetone and ethanol (Talbot and White, 2013). Microwaving samples at 750 W for one minute reduced overall dehydration time, while retaining comparable dehydration quality to the standard protocol of waiting 10 minutes at each step (Valerie Lynch-Holm, personal communication,

October 3, 2016). After three sessions of microwave irradiance in 100% methanol, the samples were subjected to a 1:1 mixture of 100% methanol and propylene oxide for ten minutes, followed by two exchanges of 100% propylene oxide for ten minutes each. The first steps of resin infiltration are lenient in terms of the time samples may be subjected to partial resin concentration (Bozzola and Russell, 1998). Embedding root tissue in 100% Spurr's resin for at least three days prior to overnight curing at 60°C improved polymer hardness for sectioning and reduced mechanical artifacts. Staining regimes are essential to increase sample contrast, but expose sections to contaminating artifacts (Stempak and Ward, 1964). Limiting staining duration to 12 minutes in 2% aqueous uranyl acetate and 6 minutes in Reynolds Lead Citrate minimized salt deposition on our thin sections.

Figure 2-1 through **Figure 2-8** demonstrate the preservation achieved in each species using our tissue preservation protocol. Root protophloem structure served as a proxy to evaluate if fixation quality was sufficient for electron microscopy. The protophloem is part of the primary phloem and, along with the metaphloem, derives from the procambium. The number of protophloem files in the central cylinder appear to be species-specific and arranged in predictable patterns. Monocots have more protophloem files in general – we observed *T. aestivum* to have eight files (**Figure 2-1B**) and *O. sativa* to have six (**Figure 2-2B**). Roots with smaller diameters tended to have fewer protophloem files, such as two in *N. tabacum* (**Figure 2-3B**), three in *M. sativa* (**Figure 2-4B**), and four protophloem files each in *I. nil* (**Figure 2-5B**) and *S. scutellarioides* (**Figure 2-6B**). The tree *C. speciosa* had five (**Figure 2-7B**) or sometimes six protophloem files. *Quercus rubra* had (**Figure 2-8B**) four protophloem files in its central cylinder

We next investigated to see if the cell neighbors of protophloem sieve elements shared a similar organization to those previously observed in *A. thaliana* (Ross-Elliott et al., 2017). We assume that branched plasmodesmata along the protophloem sieve element interface are diagnostic of a companion cell neighbor, which is usually the case (Ross-Elliott et al., 2017). In most species, root protophloem sieve elements shared cell walls with five cell neighbors, an organization that resembled the pentagonal architecture observed by Ross-Elliott et al. (2017). Conversely, *T. aestivum* (**Figure 2-1C**), *O. sativa* (**Figure 2-2C**), and *S. scutellarioides* (**Figure 2-3C**) often lacked a third vascular parenchyma cell within the stele. These species typically contained a protophloem sieve element positioned peripherally by two phloem pole pericycle cells and centrally by two companion cells. It may be that metaphloem sieve elements were not observed in transverse section in the unloading zone because the immature metaphloem sieve elements are not situated adjacent to the protophloem sieve elements immediately after differentiation from the vascular cambium.

Plasmodesmal Varieties and Distributions in the Unloading Zone

Assimilate unloading in sink tissues usually occurs through symplasmic connections provided by plasmodesmata (Patrick, 1997; Oparka, 2005). Ross-Elliott et al. (2017) described how plasmodesmata in the root unloading zone are spatially distributed along the cell walls of protophloem sieve elements in *Arabidopsis thaliana*. We found similar results, in that simple plasmodesmata are often found at the protophloem sieve element-metaphloem sieve element interface, branched plasmodesmata are abundant at the protophloem sieve element-companion cell interface, and plasmodesmata shaped like funnels are common along the protophloem sieve element-phloem pole pericycle cell interface. *T. aestivum* (**Figure 2-9**) and *O. sativa* (**Figure 2-**

10) exhibited the highest concentrations of plasmodesmata of the plants studied, whereas plasmodesmata were least frequent in *S. scutellarioides*.

Simple flow-relevant geometrical measurements are readily obtainable by selecting a subsample of plasmodesmata from TEM micrographs. The low viscous resistance of funnel plasmodesmata relative to simple and branched plasmodesmata allow fluids to pass through funnel plasmodesmata more efficiently (Ross-Elliott et al., 2017). As the main symplasmic channels for assimilate unloading into the post-phloem domain, we were interested in surveying the geometrical variability in funnel plasmodesmata across seven of our eight species as we had too few red oak micrographs. **Table 2-1** tabulates the mean measurements for the large funnel aperture radii, the small phloem pole pericycle aperture radii, and plasmodesmatal (cell wall) length measured from 30 unloading zone funnel plasmodesmata. The phloem pole pericycle aperture radius was highly consistent across plasmodesmata, only deviating by a few nanometers among the species evaluated. The plasmodesma length was also fairly uniform, as most funnel plasmodesmata measure between 300 nm and 400 nm. The funnel apertures of funnel plasmodesmata demonstrate greater radial variability, as the *O. sativa* funnel aperture radius was nearly 127 nm across while the *C. speciosa* radius was 35.5 nm across on average.

To test if an evaluator effect was skewing plasmodesma measurements, we compared the lengths recorded for 20 plasmodesmata each of *N. tabacum*, *I. nil*, and *T. aestivum* by three individuals and plotted the distributions of measured length side-by-side as histograms in **Figure 2-16**. Significant reported differences for funnel aperture ($p = 0.0004, 0.0202$), outer aperture ($p = <0.0001, <0.0001$), and cell wall thickness ($p = 0.0054, 0.0184$) measurements from *I. nil* were detected between two of the three groups, but no significant differences were found among reported measurements in *N. tabacum*, except for outer aperture radius measurements between

two individuals. Reported measurements for funnel aperture, outer aperture, and cell wall length in *T. aestivum* varied noticeably. The model assumptions of homogeneity of variance and nonnormality were violated for reported funnel aperture measurements and outer aperture measurements. This outcome was not surprising given the heterogenous nature of cell wall topology observed in *T. aestivum*. We concluded that while individual measurements of plasmodesmata on micrographs may provide a general impression of plasmodesmal geometry, obtaining accurate dimensional data of plasmodesmata requires additional information beyond static 2D images. An ideal method of measuring plasmodesma aperture sizes and other geometrical elements would involve capturing the full plasmodesma volume and evaluating pore contours as unified structures.

Figure 2-17 describes an approach of utilizing three-dimensional information contained within two-dimensional micrographs to calculate the full funnel aperture diameter of funnel plasmodesmata. The rationale of this approach derives from the fact that sections of a given thickness “fall” randomly on a funnel aperture of a given diameter. From a two-dimensional perspective, the sides of plasmodesmata apertures will appear to have “borders” or “overhangs” because cross sections situated between the middle of an aperture and tangent to the aperture carry segments of aperture curvature. By programming a large number of sections of a given thickness to fall randomly along a circle of a given diameter, and transforming the lengths of segments separating the midsection of each section to the origin of the circle using the Pythagorean theorem, it is possible to generate a distribution of predicted aperture diameters useful for quickly modeling the true aperture diameter (**Figure 2-18**). In theory, this approach requires only a small number of funnel apertures containing off-center curvature (border) information to extrapolate the true, maximum aperture diameter. Taking longitudinal sections

may seem like a simpler method of acquiring full funnel aperture diameters, however, in both cases aperture diameters are assumed to be delimited to well-defined edges along the pore curvature when no such constructs exist. While this method is compelling from a conceptual standpoint, we decided to optimize an imaging technique that takes advantage of the full volume of plasmodesmata: electron tomography.

Reconstructing Plasmodesmata Using Electron Tomography

To evaluate the full geometry of plasmodesmata as they exist in the cell wall, we employed 3D electron tomography, a technique that permits reconstruction of cellular volumes through the collection of tilting series micrographs (Toyooka and Kang, 2014). We acquired 300 to 350 nm-thick cross sections wide enough to carry the full funnel apertures of funnel plasmodesmata in the sections. To resolve the desmotubule in our reconstructions, we added 2 μL of potassium permanganate (KMnO_4) to the uranyl acetate staining solution. Potassium permanganate is an oxidizing agent that enhances membrane contrast (Sawaguchi et al., 2001). We also stained the semi-thick section in 1% aqueous tannic acid for 12 minutes in-between staining with uranyl acetate and Reynold's Lead Citrate. Tannic acid has been applied previously as a fixative and stain to resolve the ultrastructure of plasmodesmata and is particularly useful for staining the membranous desmotubule (Badelt et al., 1994). Determining the dimensions of this structure was essential because its presence contributes the hydrodynamic radius through which flow occurs in a region called the cytoplasmic sleeve (Blake, 1978). However, the permeability and flexibility of the desmotubule is not thought to influence flow rate to a large extent (Blake, 1978). We produced the reconstructions in **Figure 2-19** through **Figure 2-21** by acquiring two orthogonal single tilts in a transmission electron microscope, generating tomograms from raw tilt

stacks, and manually segmenting the tomograms to produce surface renderings using Amira Software 5.2.2 (Thermo Fisher Scientific, Waltham, Massachusetts, USA). A simple plasmodesma at the protophloem sieve element-metaphloem sieve element cell wall interface in *N. tabacum* (**Figure 2-19**) has a characteristically narrow channel through the cell wall and a wider opening at the protophloem sieve element interface. The ER of the funnel plasmodesma at the protophloem sieve element-phloem pole pericycle cell interface is more intricate as two strands of convoluted ER join above the necking region in the funnel to form the desmotubule. The *T. aestivum* funnel plasmodesma (**Figure 2-21**) has a single desmotubule that spans the pore length. The fine structure of the reconstructions are reflected in the minuscule wrinkles along the edges of the plasmodesmatal volumes. The effects of applying a more rigorous smoothing algorithm are evident when comparing the smoother edges of **Figure 2-19C** to **Figure 2-21C**. The outer apertures appear to be larger in the 3D reconstructions (50-80 nm around the desmotubule) compared to the static images from thin sections (30-35 nm). This is likely due to slightly overestimating aperture width in the 3D reconstructions during manual material labeling. The process of geometrical information extraction from plasmodesmata is enhanced by staining samples more stringently to add contrast to the tomograms because this reduces both labeling errors and processing time. Generating surface reconstructions from plasmodesmatal volumes offers a new way of visualizing the fine details of these structures.

Hydraulic Profiles of Plasmodesmata

Using the surface reconstruction of a funnel plasmodesma from *T. aestivum* as a template, we extracted a tetrahedral grid – a dataset which can operate as a functional model for flow experiments by the finite element method (Bassi and Rebay, 1997) using the flow

simulation software, Comsol Multiphysics. This analytical approach to solving complex physical problems involves the division of a larger system into simpler parts called finite elements, which can be numerically modeled and integrated back into a representative situation to generate accurate analytical solutions (Bassi and Rebay, 1997). Furthermore, internal laminar flow problems at the scale of plasmodesmata are generally solvable by finding solutions to systems of equations that describe the motion of viscous fluids called the Navier-Stokes equations (Fox and McDonald, 1985; Bassi and Rebay, 1997). In **Figure 2-22**, laminar flow through the *T. aestivum* funnel plasmodesma shows that the velocity increases in the vessel centerline with distance from the inlet funnel aperture – a result which satisfies the continuity equation for incompressible fluids (Fox and McDonald, 1985). Fluid along the internal surfaces of the plasmodesma is assumed to be static, forming a no-slip boundary layer (Fox and McDonald, 1985). Wall friction retards flow rate and velocity, especially near the narrow phloem pole pericycle (outer) aperture where the boundary layer formed off of the wall exerts shearing forces into the center streamline, producing the highest viscosity near the outer aperture (Fox and McDonald, 1985). Flow velocity through the outer aperture is higher (~0.05 m/s) than the inlet flow velocity (~0.015 m/s) because the same volume of fluid must pass through a smaller area for flow to be continuous (Fox and McDonald, 1985). Considering Hagan-Poiseuille equation of hydraulic resistance, the high viscosity (η) of flow in the outer aperture and its narrow width (r), this region of the plasmodesma would be expected to cause nearly all of the resistance to flow through the pore (Fox and McDonald, 1985).

Discussion

Tissue Fixation Procedure

Our approach of investigating the root protophloem unloading network began by tailoring an established tissue preservation protocol for electron microscopy to prepare roots of relatively large diameter (~0.5 mm – 1.2 mm) for structural analysis. A fixative formulation of 2% paraformaldehyde and 2% glutaraldehyde yielded the best results when buffered by 0.05 M sodium cacodylate (pH 7.2) and irradiated briefly at 750 W. High-pressure freeze and freeze substitution have replaced traditional chemical fixation in many labs, as these methods accomplish fixation swiftly and often generate fewer artifacts (Austin, 2014). These techniques are recommended for tissues 0.3 mm or smaller in thickness, however, due to the buildup of ice crystals deeper in the tissue (Austin, 2014). While these techniques may be suitable for *N. tabacum*, they are non-optimal or prohibitory for the other roots investigated due to the deeply situated protophloem. Incubation time in OsO₄ emerged as a decisive stage of preservation quality. Failing to osmicate *T. aestivum* and *O. sativa* roots a second time or subjecting *S. scutellarioides* roots to additional osmium tetroxide treatment rendered them useless due to poor fixation.

Imaging Workflow

Our images of protophloem ultrastructure and plasmodesmata offer a preview of the conservation in cellular architecture in the protophloem unloading zone, but also adaptations in the geometry of these structures. The height of bifurcation of plasmodesmal branches and especially funnel aperture diameters of funnel plasmodesmata seem subtle at first glance, but

may likely apply dramatic effects on symplasmic unloading conductance when assessed for cumulative effects.

In practice, charting plasmodesmata abundance through manual serial sectioning and imaging is relatively inefficient, especially since precisely modeling phloem unloading should capture each of the potentially hundreds of plasmodesmata in each protophloem sieve element. High-throughput serial block-face scanning electron microscopy (SBFSEM) is an innovative platform that is capable of collecting large numbers of plasmodesmata, along with their spatial distributions (Meschini, 2017). Ross-Elliott et al. (2017) mapped the volumes of six complete protophloem sieve elements, comprising of 2100 serial transverse sections, with the aid of this technique. Collecting 3D volumes of protophloem sieve files from each of the angiosperm roots investigated would provide us with the datasets needed to model if convective phloem unloading describes the unloading mechanism in the plant roots we studied, as it does in *A. thaliana* (Ross-Elliott et al., 2017).

Our 3D reconstructions of plasmodesmata appear to be the first of their kind. Generating more repetitions and reconstructing more plasmodesma varieties will shed light on the diversity of plasmodesmata within and between plant species. Enhancing the contrast of plasmodesmata for tomography will be necessary to provide more accurate flow models, as applying algorithms to detect fine structure like endoplasmic reticulum and the desmotubule from background would reduce mislabeling due to bias. However, our experience segmenting these structures demonstrate that manual labeling is necessary at this stage because the desmotubule signal was quite faint.

Modeling Symplasmic Unloading

Generating reconstructions from authentic plasmodesmata as they exist in the cell wall to study hydraulic conductance brings quantitative analysis of phloem unloading to a new level. The precision of data gathered by finite element analysis of electron tomography-generated 3D datasets is unmatched, yet the demanding nature of extracting individual plasmodesmata for analysis is prohibitive for investigating large numbers of structures. Comparing the hydraulic profiles of a small sample of plasmodesmata from our species should yield the flow relevant parameters necessary to test if convective phloem unloading is widespread, following the modeling procedure described in Ross-Elliott et al. (2017). The analysis of sieve element hydrodynamics outlined by Jensen et al. (2012) provides another innovative approach to understanding phloem unloading. In their investigation, Jensen et al. (2012) applied Kirchhoff's circuit laws to model the serial hydraulic resistance contributed by both sieve element lumens and sieve plates. Alternatively, the relative hydraulic conductance of plasmodesmata may be attainable by viewing plasmodesmata as parallel hydraulic capacitors.

Future experiments related to phloem unloading may involve manipulating the program of symplasmic regulation. Whereas long-term control of symplasmic unloading is achieved by modifying the numbers of plasmodesmata, plants have shown to regulate symplasmic unloading in the short term by modifying plasmodesmatal radii to attenuate pore conductance, likely through the action of callose synthase (Patrick, 1997; Oparka, 2005). Modifying the factors involved in shaping plasmodesmata geometry are promising targets for designing more productive crops.

Materials and Methods

Plant material and growth conditions

All plants were grown by seed in pots of soil under 60 to 70% relative humidity and watered daily. Daytime irradiance lasted 14 hours. A lamp fixture [model #PL 90 (PL Lighting Systems, Ontario, Canada)] provided a minimum of $150 \mu\text{E m}^{-2} \text{s}^{-1}$ of irradiance at night. Plants were maintained at maturity to provide a ready supply of root tips. A list of seed stocks and their suppliers follows – *Triticum aestivum* (www.sustainableseedsco.com), *Oryza sativa* (Thomas Sexton of Cousins Lab, Pullman, WA), *Nicotiana tabacum* (Knoblauch Lab, Pullman, WA), *Medicago sativa* (Chris's Garden webpage on www.amazon.com), *Ipomoea nil* (Knoblauch Lab, Pullman, WA), *Solenostemon scutellarioides* (Abelson Greenhouse, Pullman, WA), *Catalpa speciosa* (www.hobbyseeds.com), and *Quercus rubra* (www.arborday.org).

Sample preparation

Primary root tip segments of about 3 mm in length were excised from mature plants and swiftly transferred into cold 0.05 M cacodylate-buffered fixative solutions containing 2% paraformaldehyde and 2% glutaraldehyde. Microwave treatments consisted of two 90-second sessions of irradiance at 750 W of power, with a one-minute pause after the first session. Sample vials were incubated in an ice bath during this process. After washing samples with water three times for ten minutes each, the roots were subjected to overnight post-fixation in 1% OsO₄ at 4 °C. After washing, some roots were subjected to additional osmication as described above. A graded methanol dehydration series (10% steps, three rounds in 100% methanol) with microwave assistance (750 W irradiation for 1 minute at each step) was followed by two exchanges of 100% propylene oxide, each 10 minutes. Daily exchanges of increasing propylene

oxide to Spurr's resin followed a schedule of 1:3, 1:2: 1:1, and 2:1. Samples were embedded in Spurr's resin for 3 days before curing overnight at 60 °C. Thick and thin sections were obtained with glass knives. Thick sections were stained for 30 seconds with toluidine blue with 1% borax on a heat plate and imaged in tiles on a Leica DM LSFA microscope. Thin section of 80 nm were obtained and stained with 2% uranyl acetate, rinsed with ddH₂O, stained with Reynold's Lead Citrate, and rinsed a final time before imaging. Semi-thick 300 or 350 nm thick sections were obtained and stained the same way as the thin sections, except 2 µL KMnO₄ was added to the uranyl acetate stain and a 12-minute step of staining in 1% tannic acid with a subsequent water rinse was incorporated. All stains were filtered through 0.2 µm pore PES membrane filters.

Electron Microscopy and Tomography

Electron micrographs and raw tilt series for electron tomography were acquired using a Tecnai FEI T20 transmission electron microscope equipped with a 200 kV electron gun. Gold fiducial markers 15 nm in diameter were added to the semi-thick sections for tomography. Tilt series were collected in 2° increments up to ±60°. Tomogram processing and combination was carried out using the eTomo application of the IMOD software package (Kremer et al., 1996; Mastronarde, 1997; Mastronarde, 2017). Final tomograms had voxel sizes of 0.3575.

Plasmodesmata reconstructions and Flow Simulations

Tomograms were resampled and manually segmented on Amira software. Subsequent label fields were reconstructed into surfaces and geometrically optimized. The *T. aestivum* plasmodesma surface was converted into a grid file and subjected to flow simulations on Comsol Multiphysics 5.4 (Comsol Multiphysics, Inc., Burlington Massachusetts, USA). The inlet

pressure at the funnel aperture was 2 atm, while the outlet pressure from the outer aperture was 1 atm. The cylinders covering the inlet and outlet had a length of roughly 10x larger than the diameter of the inlet to dissipate boundary flows. The grid used for flow simulation was constructed in AutoCAD software (Autodesk, Inc., San Rafael, California, USA) because the grid from the Amira platform did not translate properly.

Image and Data Processing Software

Images were optimized for visualization and compiled using GIMP 2.8.18 (GNU Image Manipulation Program, Creative Commons Attribution-ShareAlike 4.0 International License). Plasmodesmata measurements were completed using ImageJ 1.50i (National Institutes of Health, USA). Measures of central tendency and graphs were obtained using Excel 2016 (Microsoft Office 365). Analyses of variance were computed using SAS University Edition (SAS Institute, Inc., Cary, North Carolina, USA). Plasmodesma measurements were organized into completely randomized block designs and subjected to one-way ANOVA to investigate the effects of evaluator on perceived plasmodesma edges.

Author Contributions

GPO, Acquisition of data, Analysis and interpretation of data, Collected samples, Modified conceptual models, Managed the overall experimental strategy, Wrote the manuscript; WSP, Generated aperture diameter modeling concept, Revised manuscript; ARF, Performed flow simulations; KHJ, Managed flow simulations; MK, Designed the overall experimental strategy, Evaluated experimental design.

Acknowledgements

Our investigation was funded using a National Science Foundation grant number IOS 1146500 (MK). We are grateful for the personnel support and instrumentation access provided by the Franceschi Microscopy and Imaging Center at Washington State University. We thank the Department of Physics at the Technical University of Denmark for the personnel and computational resources used to produce flow simulations. The authors declare no competing financial interests.

Tables

Table 2-1. A comparison of funnel plasmodesmata dimensions in various roots relative to *Arabidopsis thaliana*. N = 30 for each sample mean.

Species	Funnel Radius (nm)	Outer Radius (nm)	PD Length (nm)
<i>A. thaliana</i> (Ross-Elliott et al., 2017)	75.0	10.3	500
<i>T. aestivum</i>	68.1	17.5	296.4
<i>O. sativa</i>	126.9	17.2	313.9
<i>N. tabacum</i>	51.6	12.6	308.6
<i>M. sativa</i>	56.7	16.3	379.3
<i>I. nil</i>	90.5	15.0	320.6
<i>S. scutellarioides</i>	56.8	14.4	383.1
<i>C. speciosa</i>	35.5	17.7	334.0

Figures

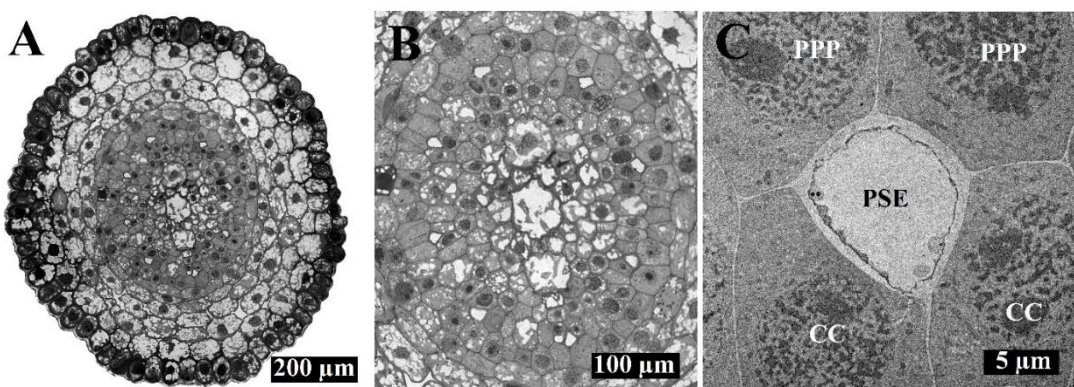


Figure 2-1. Cross sectional view of the root unloading zone of *Triticum aestivum*. (A) Overview of a *T. aestivum* root. (B) Eight functional protophloem files are present in the central cylinder. (C) Delivery of phloem contents is mediated by the protophloem sieve element. In *T. aestivum*, the most frequently observed neighbors of the protophloem sieve element are two peripheral phloem pole pericycle cells and two central companion cells. PSE, protophloem sieve element; PPP, phloem pole pericycle; CC, companion cell.

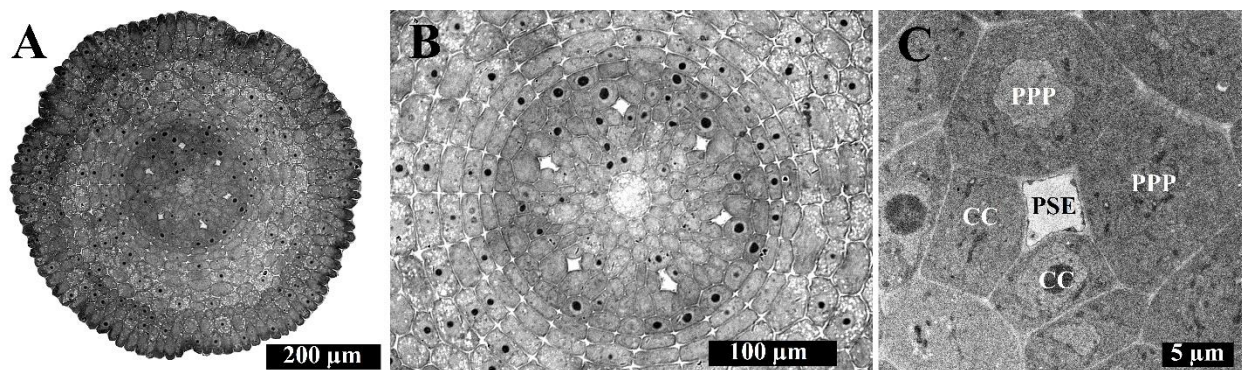


Figure 2-2. Cross sectional view of the root unloading zone of *Oryza sativa*. (A) Overview of an *O. sativa* root. (B) Six functional protophloem files are present in the central cylinder. (C) Delivery of phloem contents is mediated by the protophloem sieve element. In *O. sativa*, the most frequently observed neighbors of the protophloem sieve element are two peripheral phloem pole pericycle cells and two central companion cells. PSE, protophloem sieve element; PPP, phloem pole pericycle; CC, companion cell.

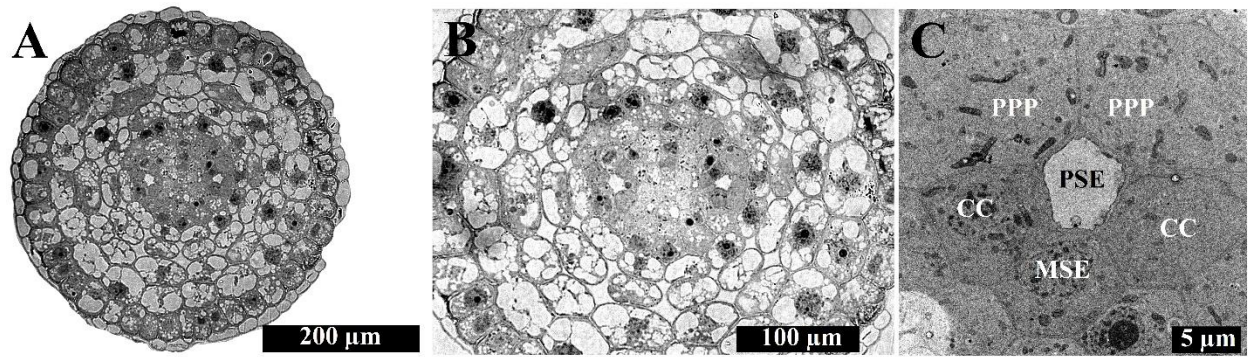


Figure 2-3. Cross sectional view of the root unloading zone of *Nicotiana tabacum*. (A) Overview of a *N. tabacum* root. (B) Two functional protophloem files are present in the central cylinder. (C) Delivery of phloem contents is mediated by the protophloem sieve element. In *N. tabacum*, the most frequently observed neighbors of the protophloem sieve element are two peripheral phloem pole pericycle cells, two lateral companion cells, and one central metaphloem sieve element cell. PSE, protophloem sieve element; PPP, phloem pole pericycle; CC, companion cell; MSE, metaphloem sieve element.

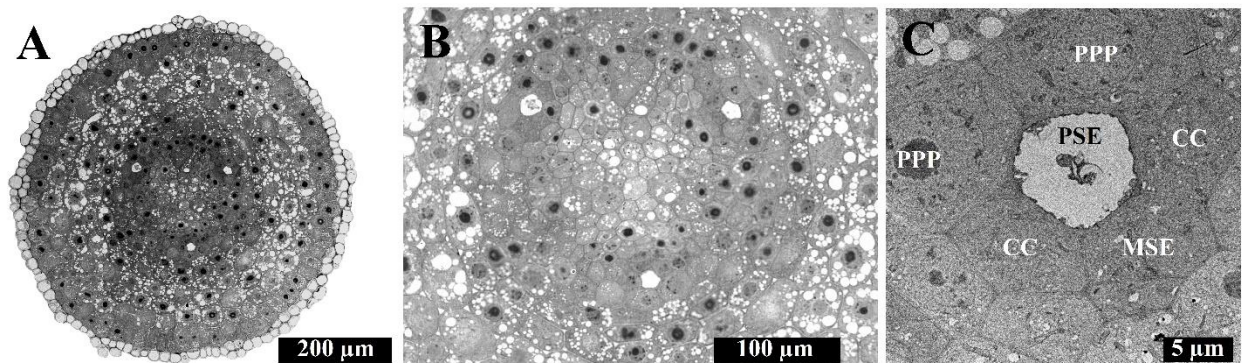


Figure 2-4. Cross sectional view of the root unloading zone of *Medicago sativa*. (A) Overview of a *M. sativa* root. (B) Three functional protophloem files are present in the central cylinder. (C) Delivery of phloem contents is mediated by the protophloem sieve element. In *M. sativa*, the most frequently observed neighbors of the protophloem sieve element are two peripheral phloem pole pericycle cells, two lateral companion cells, and one central metaphloem sieve element cell. PSE, protophloem sieve element; PPP, phloem pole pericycle; CC, companion cell; MSE, metaphloem sieve element.

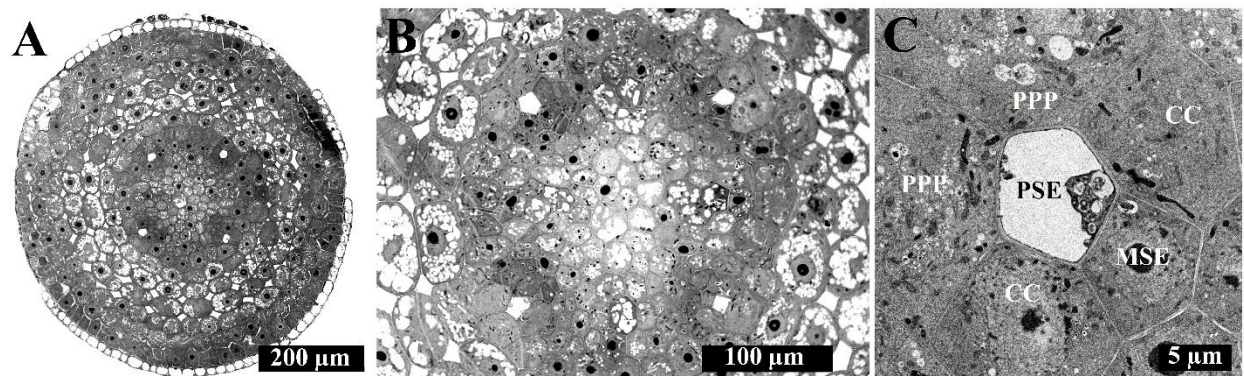


Figure 2-5. Cross sectional view of the root unloading zone of *Ipomoea nil*. (A) Overview of an *I. nil* root. (B) Four functional protophloem files are present in the central cylinder. (C) Delivery of phloem contents is mediated by the protophloem sieve element. In *I. nil*, the most frequently observed neighbors of the protophloem sieve element are two peripheral phloem pole pericycle cells, two lateral companion cells, and one central metaphloem sieve element cell. PSE, protophloem sieve element; PPP, phloem pole pericycle; CC, companion cell; MSE, metaphloem sieve element.

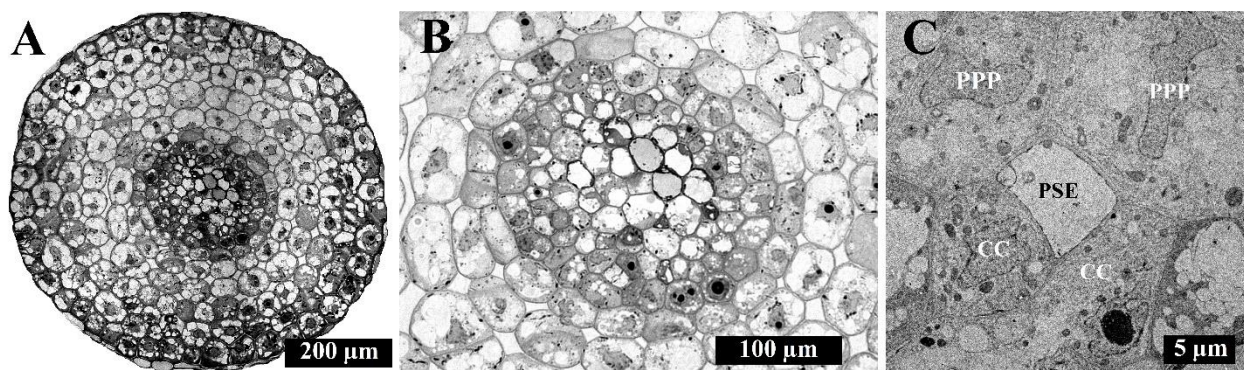


Figure 2-6. Cross sectional view of the root unloading zone of *Solenostemon scutellarioides*. (A) Overview of a *S. scutellarioides* root. (B) Four functional protophloem files are present in the central cylinder. (C) Delivery of phloem contents is mediated by the protophloem sieve element. In *S. scutellarioides*, the most frequently observed neighbors of the protophloem sieve element are two peripheral phloem pole pericycle cells and two central companion cells. PSE, protophloem sieve element; PPP, phloem pole pericycle; CC, companion cell; MSE, metaphloem sieve element.

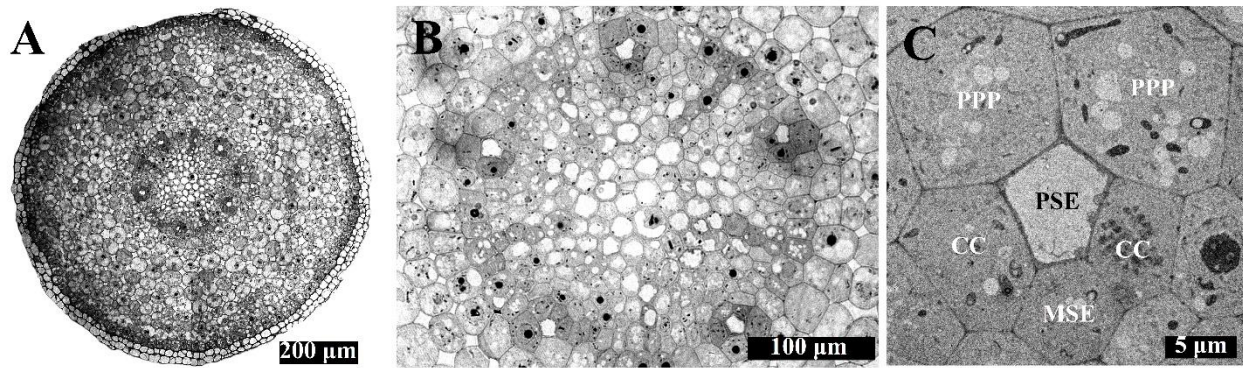


Figure 2-7. Cross sectional view of the root unloading zone of *Catalpa speciosa*. (A) Overview of a *C. speciosa* root. (B) Five functional protophloem files are present in the central cylinder. (C) Delivery of phloem contents is mediated by the protophloem sieve element. In *C. speciosa*, the most frequently observed neighbors of the protophloem sieve element are two peripheral phloem pole pericycle cells, two lateral companion cells, and one central metaphloem sieve element cell. PSE, protophloem sieve element; PPP, phloem pole pericycle; CC, companion cell; MSE, metaphloem sieve element.

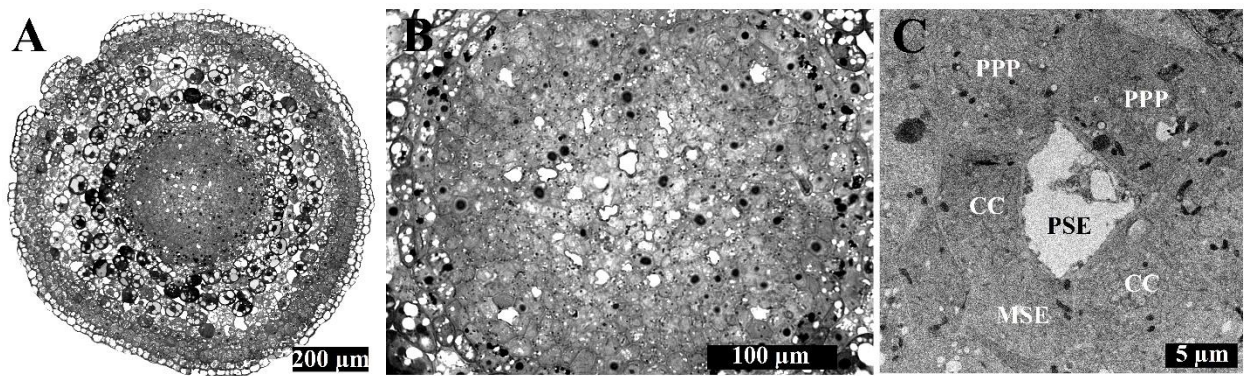


Figure 2-8. Cross sectional view of the root unloading zone of *Quercus rubra*. (A) Overview of a *Q. rubra* root. (B) Four functional protophloem files are present in the central cylinder. (C) Delivery of phloem contents is mediated by the protophloem sieve element. In *Q. rubra*, the most frequently observed neighbors of the protophloem sieve element are two peripheral phloem pole pericycle cells, two lateral companion cells, and one central metaphloem sieve element cell, although this pattern appeared less consistently than in the other species investigated. PSE, protophloem sieve element; PPP, phloem pole pericycle; CC, companion cell; MSE, metaphloem sieve element.

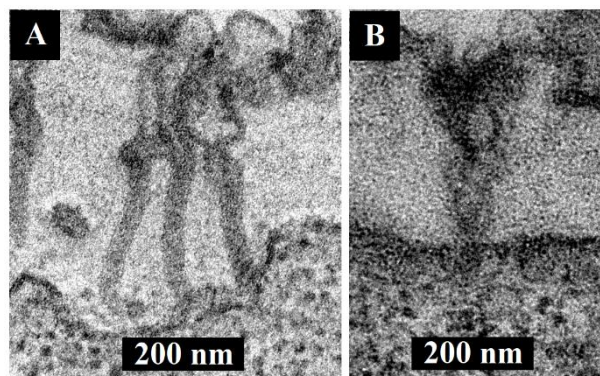


Figure 2-9. Plasmodesma varieties present in the root protophloem sieve element cell walls of *Triticum aestivum*. (A) A branched plasmodesma linking a protophloem sieve element (above cell wall) to a companion cell (below cell wall). (B) A funnel plasmodesma linking a protophloem sieve element (above cell wall) to a phloem pole pericycle cell (below cell wall).

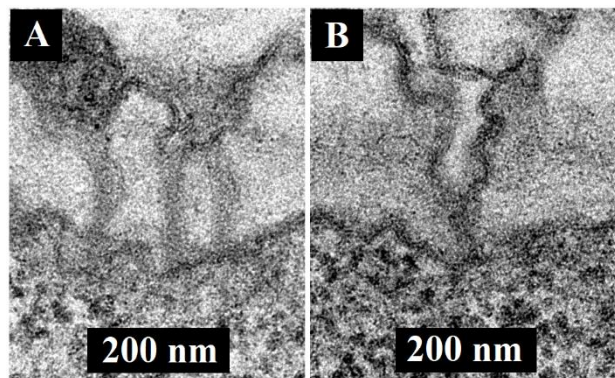


Figure 2-10. Plasmodesma varieties present in the root protophloem sieve element cell walls of *Oryza sativa*. (A) A branched plasmodesma linking a protophloem sieve element (above cell wall) to a companion cell (below cell wall). (B) A funnel plasmodesma linking a protophloem sieve element (above cell wall) to a phloem pole pericycle cell (below cell wall).

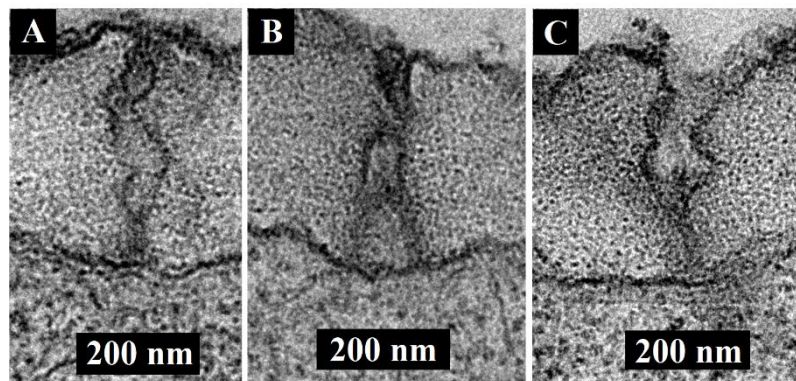


Figure 2-11. Plasmodesma varieties present in the root protophloem sieve element cell walls of *Nicotiana tabacum*. A simple plasmodesma linking a protophloem sieve element (above cell wall) to a metaphloem sieve element (below). (B) A branched plasmodesma linking a protophloem sieve element (above cell wall) to a companion cell (below cell wall). (B) A funnel plasmodesma linking a protophloem sieve element (above cell wall) to a phloem pole pericycle cell (below cell wall).

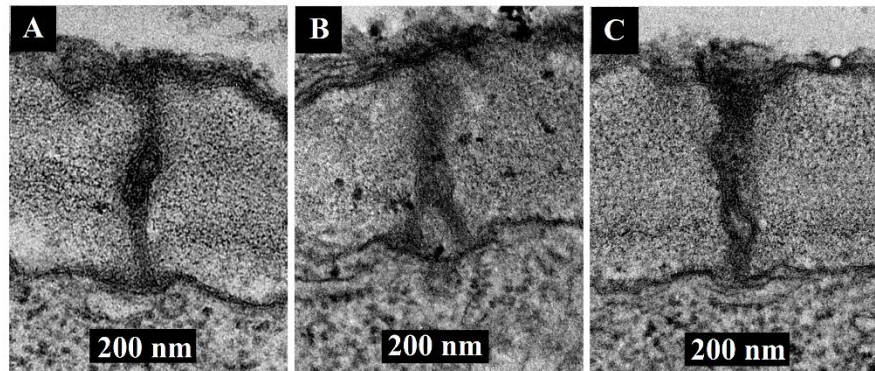


Figure 2-12. Plasmodesma varieties present in the root protophloem sieve element cell walls of *Medicago sativa*. A simple plasmodesma linking a protophloem sieve element (above cell wall) to a metaphloem sieve element (below). (B) A branched plasmodesma linking a protophloem sieve element (above cell wall) to a companion cell (below cell wall). (B) A funnel plasmodesma linking a protophloem sieve element (above cell wall) to a phloem pole pericycle cell (below cell wall).

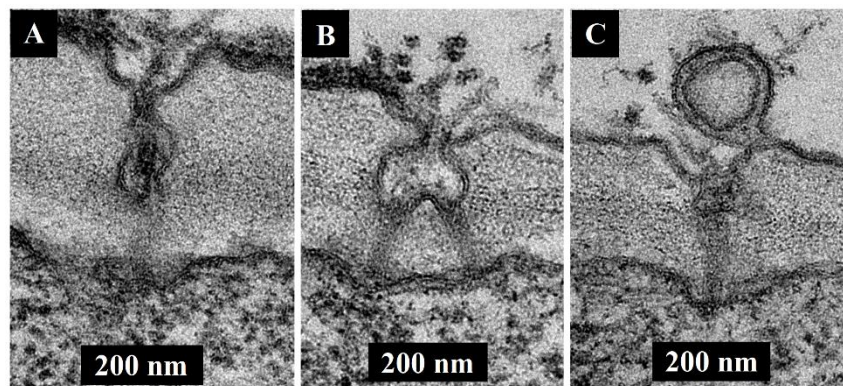


Figure 2-13. Plasmodesma varieties present in the root protophloem sieve element cell walls of *Ipomoea nil*. A simple plasmodesma linking a protophloem sieve element (above cell wall) to a metaphloem sieve element (below cell wall). (B) A branched plasmodesma linking a protophloem sieve element (above cell wall) to a companion cell (below cell wall). (B) A funnel plasmodesma linking a protophloem sieve element (above cell wall) to a phloem pole pericycle cell (below cell wall).

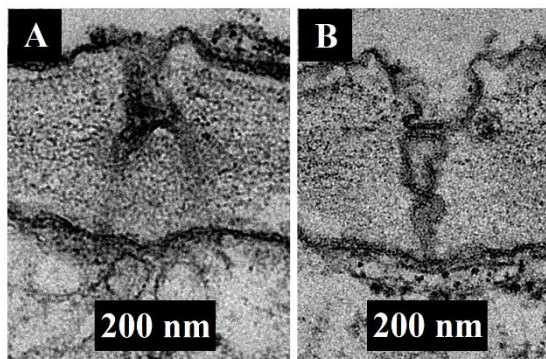


Figure 2-14. Plasmodesma varieties present in the root protophloem sieve element cell walls of *Solenostemon scutellarioides*. (A) A branched plasmodesma linking a protophloem sieve element (above cell wall) to a companion cell (below cell wall). (B) A funnel plasmodesma linking a protophloem sieve element (above cell wall) to a phloem pole pericycle cell (below cell wall).

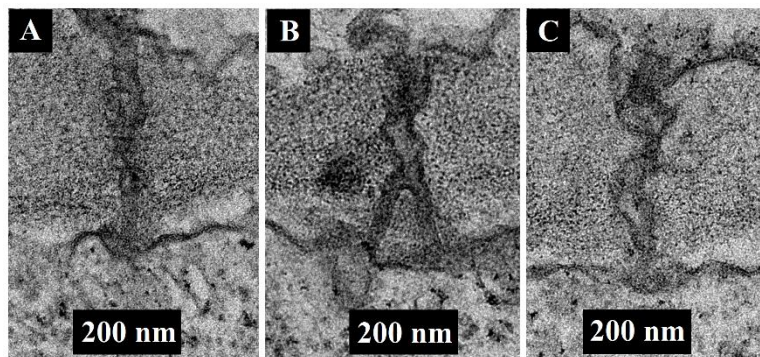


Figure 2-15. Plasmodesma varieties present in the root protophloem sieve element cell walls of *Catalpa speciosa*. A simple plasmodesma linking a protophloem sieve element (above cell wall) to a metaphloem sieve element (below cell wall). (B) A branched plasmodesma linking a protophloem sieve element (above cell wall) to a companion cell (below cell wall). (B) A funnel plasmodesma linking a protophloem sieve element (above cell wall) to a phloem pole pericycle cell (below cell wall).

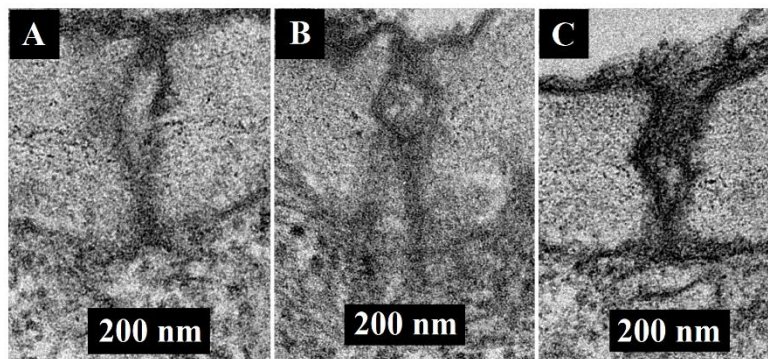


Figure 2-15. Plasmodesma varieties present in the root protophloem sieve element cell walls of *Quercus rubra*. A simple plasmodesma linking a protophloem sieve element (above cell wall) to a metaphloem sieve element (below cell wall). (B) A branched plasmodesma linking a protophloem sieve element (above cell wall) to a companion cell (below cell wall). (B) A funnel plasmodesma linking a protophloem sieve element (above cell wall) to a phloem pole pericycle cell (below cell wall).

Plasmodesma Measurements

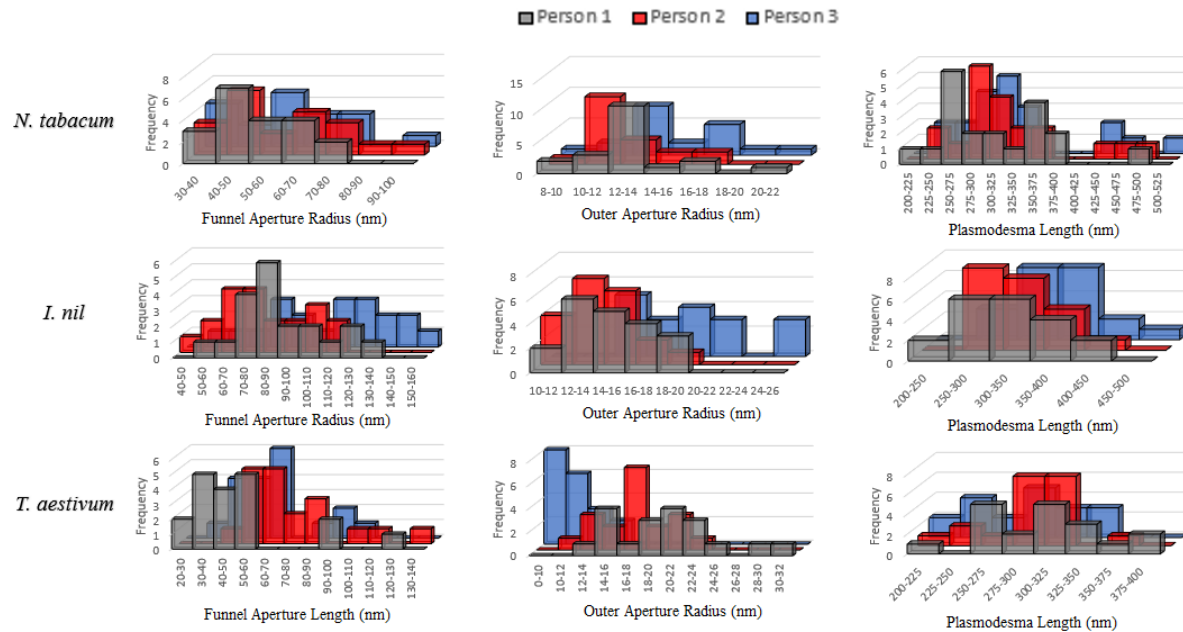


Figure 2-16. Variation in independent measurements performed on plasmodesmata.
Measurements of aperture radii and cell wall thickness for three plant species (*Nicotiana tabacum*, *Ipomoea nil*, and *Triticum aestivum*) by three individuals were compared to investigate the contribution of evaluator perception on reported values.

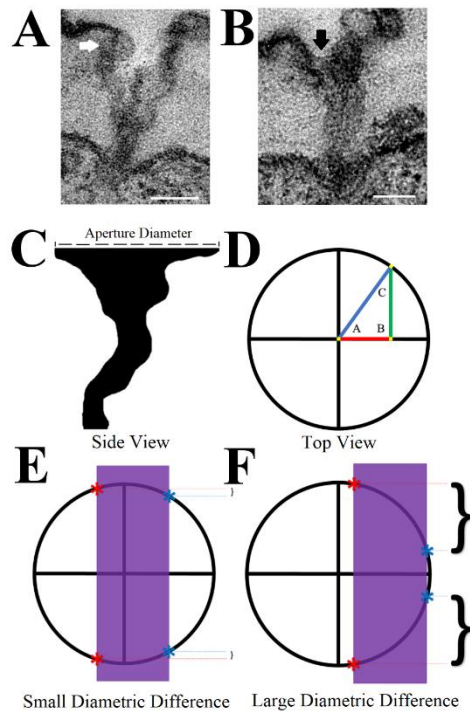


Figure 2-17. Conceptual approach to modeling aperture diameters in funnel plasmodesmata using micrographs that contain obscure and incomplete information. (A-B) Archetypical funnel plasmodesmata in the protophloem sieve element-phloem pole pericycle cell wall interface of *Triticum aestivum*. (A) Defining the funnel aperture boundary of a funnel plasmodesma is problematic when obstructive materials are present at the funnel aperture margins (white arrow). (B) One implication of the constraint of imaging partial volumes of plasmodesmata is that sections fall randomly along the funnel aperture. This funnel plasmodesma captured in an 80 nm thin section exhibits curvature (black arrow) but may not exhibit the true full diameter of the funnel aperture. (C) Silhouette of a funnel plasmodesma observed in a cross section. (D-F) Theoretical funnel apertures, assuming the contours of a large number of funnel apertures converge to a circle. (D) Top view of a funnel aperture. Line segments formed by points A, B, and C subtend the angles of a Pythagorean triangle. AB represents the distance between the origin and the midline of a thin section. BC represents the radius length of a funnel aperture observed in a thin section. AC represents the true diameter of a funnel aperture. (E) A thin section (purple) of a given thickness may capture plasmodesma volume near the center of the funnel aperture, resulting in thin borders at the funnel aperture margins. Thin borders correspond to a small difference between observed and predicted funnel aperture diameters. (F) A thin section may alternatively capture plasmodesma volume near the edge of the funnel aperture, resulting in thick borders at the funnel aperture margins. Thick borders correspond to a large difference between observed and predicted funnel aperture diameters. PSE, protophloem sieve element; PPP, phloem pole pericycle cell. Scale bars: A, B = 100 nm.

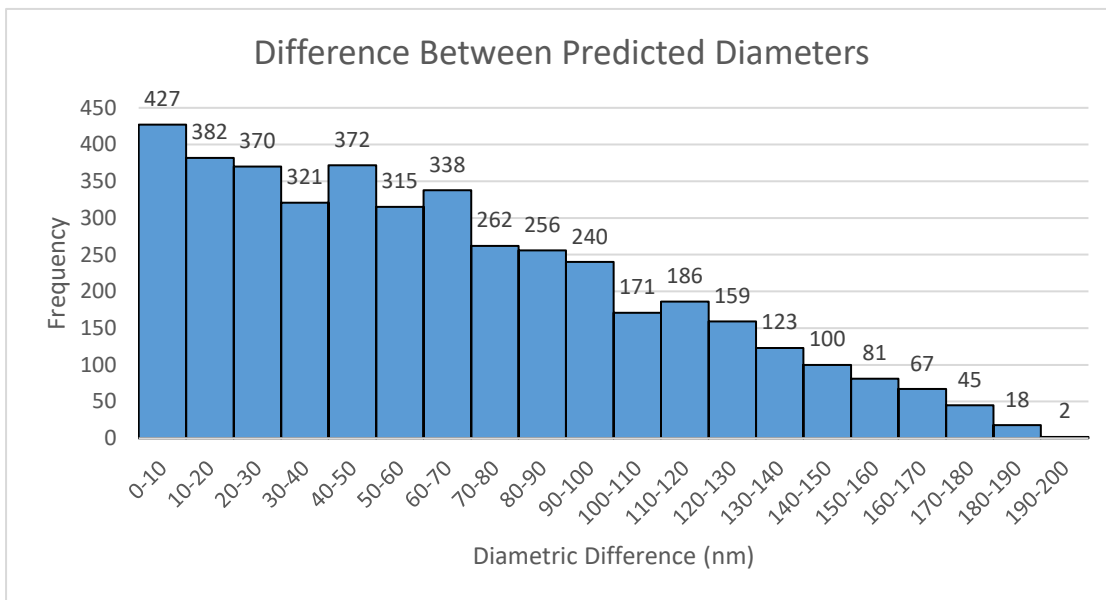


Figure 2-18. Distribution of predicted border lengths present at the margins of a large number of funnel plasmodesmata funnel apertures. Simulating 10,000 randomly positioned thin sections of a given thickness (80 nm) across a circular funnel aperture of a given diameter (200 nm) produces a histogram of predicted border lengths that reveals a trend of larger funnel aperture borders appearing less frequently. Approximately 57% of the iterations resulted in thin sections containing funnel apertures with no marginal borders.

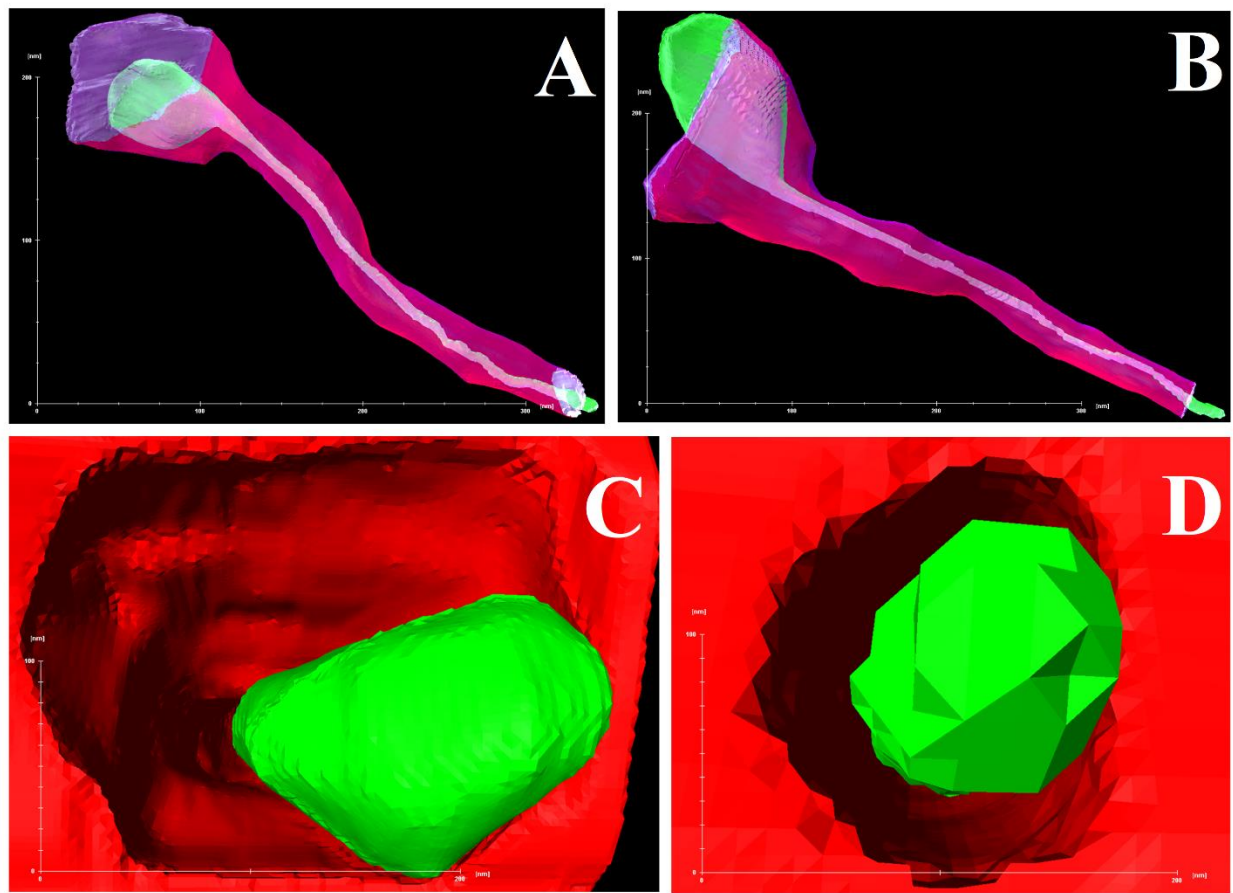


Figure 2-19. Three-dimensional reconstruction of a simple plasmodesma at the protophloem sieve element-metaphloem sieve element cell wall interface in *Nicotiana tabacum*. (A-B) Reconstruction side views. (C) Protophloem sieve element aperture. (D) Phloem pole pericycle cell aperture. Plasmodesmatal volume is rendered in purple/pink, ER/desmotubule is rendered in green, and the cell wall is rendered in red.

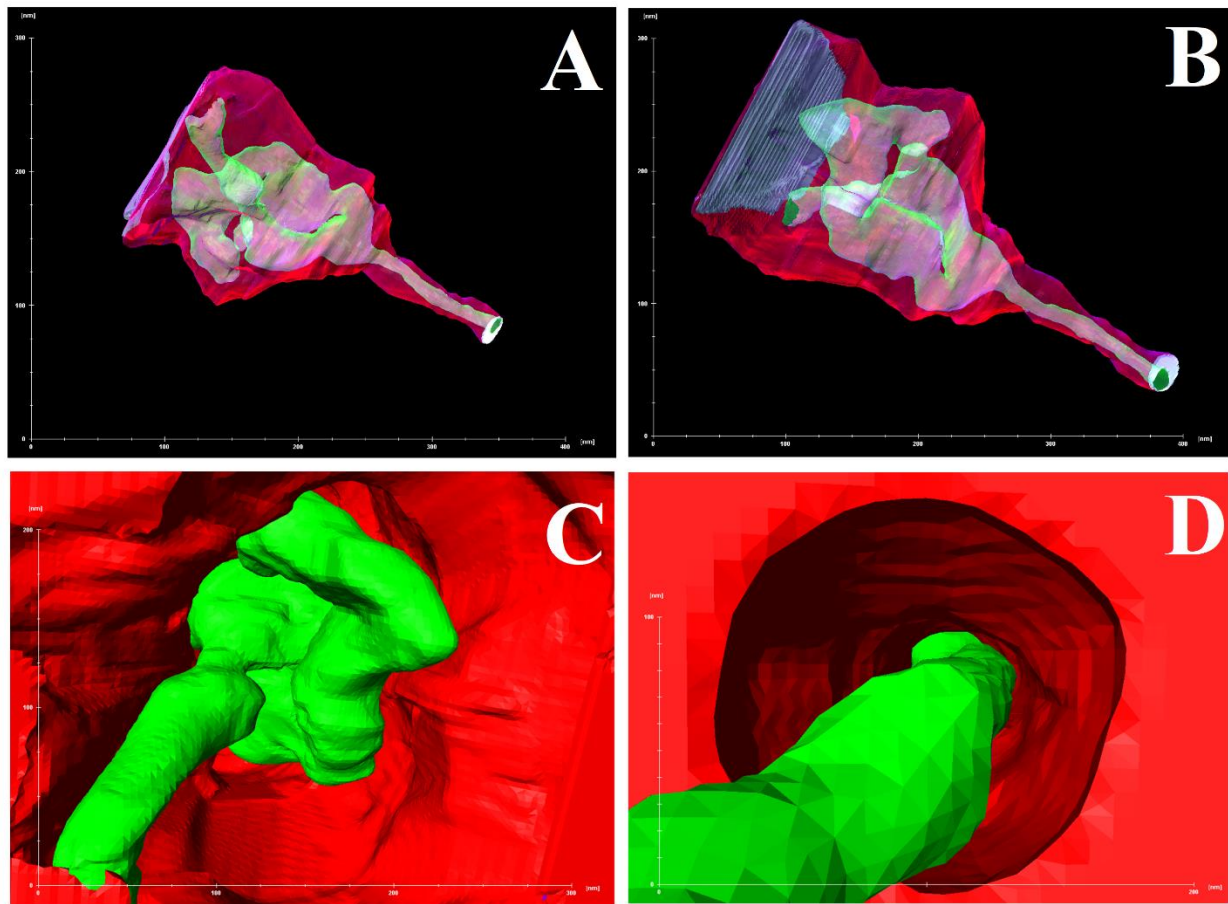


Figure 2-20. Three-dimensional reconstruction of a simple plasmodesma at the protophloem sieve element-phloem pole pericycle cell wall interface in *Nicotiana tabacum*. (A-B) Reconstruction side views. (C) Protophloem sieve element aperture. (D) Phloem pole pericycle cell aperture. Plasmodesmatal volume is rendered in purple/pink, ER/desmotubule is rendered in green, and the cell wall is rendered in red.

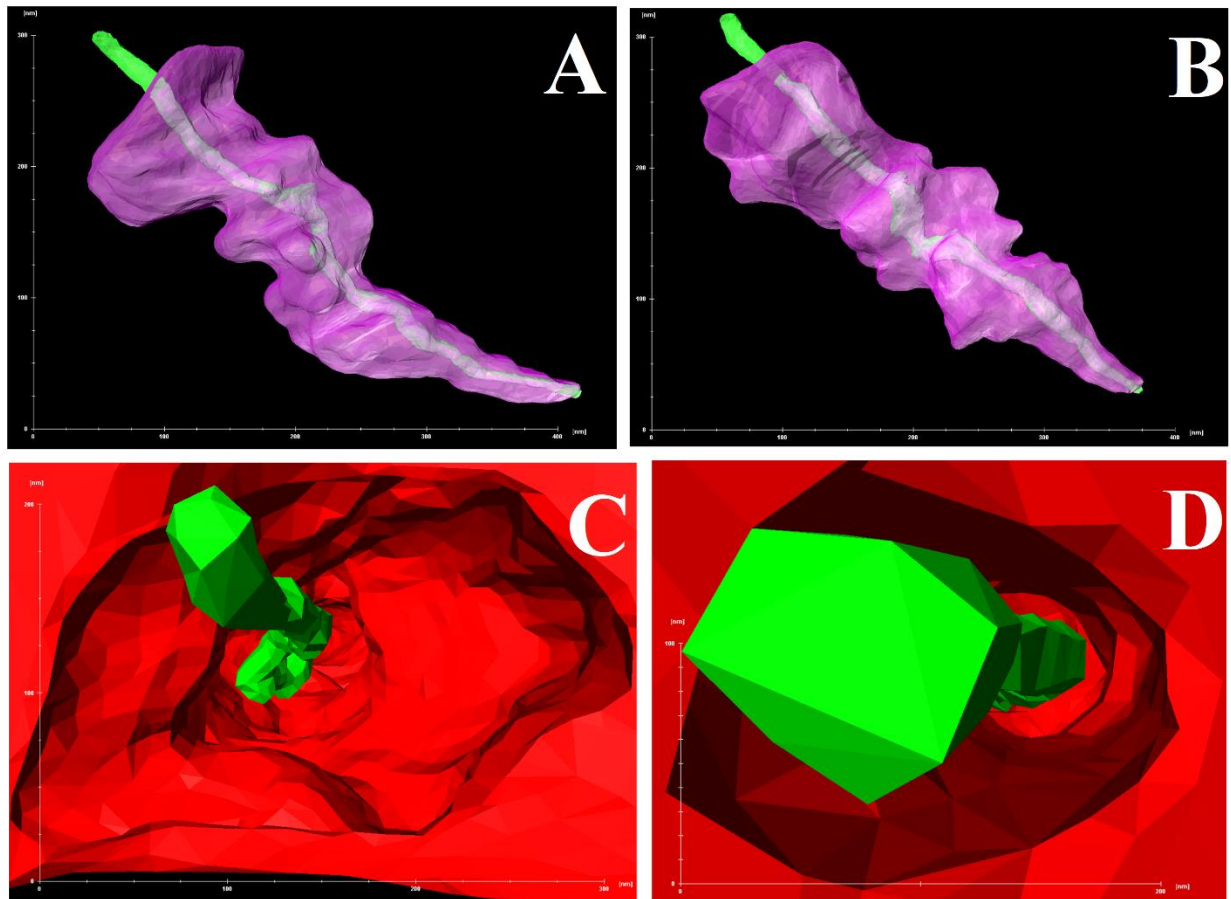


Figure 2-21. Three-dimensional reconstruction of a simple plasmodesma at the protophloem sieve element-phloem pole pericycle cell wall interface in *Triticum aestivum*. (A-B) Reconstruction side views. (C) Protophloem sieve element aperture. (D) Phloem pole pericycle cell aperture. Plasmodesmatal volume is rendered in purple/pink, ER/desmotubule is rendered in green, and the cell wall is rendered in red.

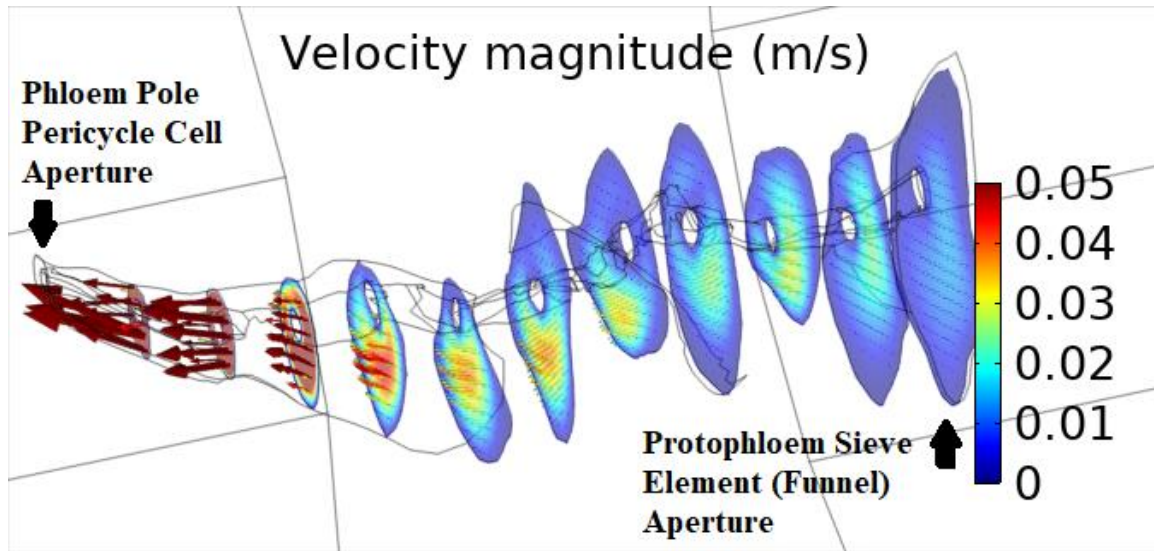


Figure 2-22. Laminar flow through a *Triticum aestivum* funnel plasmodesma. Flow velocity increases towards the outer phloem pole pericycle aperture due to the narrower vessel diameter.

REFERENCES

- Austin JR.** 2014. High-pressure freezing and freeze substitution of arabidopsis for electron microscopy. *Methods in Molecular Biology – Arabidopsis Protocols* **1062**:473–486. DOI: 10.1007/978-1-62703-580-4_25
- Badelt K**, White RG, Overall RL, Vesk M. 1994. Ultrastructural specializations of the cell wall sleeve around plasmodesmata. *Structure and Development* **81**:1422–1427. DOI: 10.1002/j.1537-2197.1994.tb15628.x
- Bais HP**, Loyola-Vargas VM, Flores HE, Vivanco JM. 2001. Root-specific metabolism: The biology and biochemistry of underground organs. *In Vitro Cellular & Developmental Biology – Plant* **37**:730–741. DOI: 10.1079/IVP2001232
- Barham L**, Mitchell, P. 2008. *The first africans: African archaeology from the earliest toolmakers to most recent foragers*. Oxford, UK: Oxford University Press
- Bassi F**, Rebay S. 1997. A high-order accurate discontinuous finite element method for the numerical solution of the compressible navier-stokes equations. *Journal of Computational Physics* **131**:267–279. DOI: 10.1006/jcph.1996.5572
- Bauby H**, Divol F, Truernit E, Grandjean O, Palauqui JC. 2007. Protophloem differentiation in early arabidopsis thaliana development. *Plant and Cell Physiology* **48**:97–109. DOI: 10.1093/pcp/pcl045
- Bell K**, Oparka K. 2011. Imaging plasmodesmata. *Protoplasma* **248**:9–25. DOI: 10.1007/s00709-010-0233-6
- Bennett M**. 1994. Plants and people in oral tradition: Folklore in the scottish highlands. *Journal of the Botanical Society of Scotland* **4**:688–692. DOI: 10.1080/13594869409441782
- Bessey CE**. 1915. The phylogenetic taxonomy of flowering plants. *Annals of the Missouri Botanical Garden* **2**:109–164. DOI: 10.2307/2990030
- Baker RF**, Leach KA, Boyer NR, Swyers MJ, Benitez-Alfonso Y, Skopelitis T, Luo A, Sylvester A, Jackson D, Braun DM. 2016. Sucrose transporter zmsut1 expression and localization uncover new insights into sucrose phloem loading. *Plant Physiology* **172**:1876–1898. DOI: 10.1104/pp.16.00884
- Blake JR.** 1978. On the hydrodynamics of plasmodesmata. *Journal of Theoretical Biology* **74**:33–47. DOI: 10.1016/0022-5193(78)90288-6
- Blake JR.** 1977. Transport in sieve tubes and plasmodesmata.
- Bozzola JJ**, Russell LD. 1998. *Electron Microscopy: Principles and Techniques for Biologists*, 2nd Ed.. Sudbury, Massachusetts, USA: Jones and Bartlett

- Brenner R.** 1976. Agrarian class structure and economic development in pre-industrial europe. *Past & Present* **70**:30–75. DOI: 10.1093/past/70.1.30
- Brunkard JO**, Runkel AM, Zambryski PC. 2015. The cytosol must flow: Intercellular transport through plasmodesmata. *Current Opinion in Cell Biology* **35**:13–20. DOI: 10.1016/j.ceb.2015.03.003
- Bruus H.** 2008. *Theoretical Microfluidics*. Oxford, UK: Oxford University Press
- Carlsson K**, Danielsson PE, Lenz R, Liljeborg A, Majlöf L, Åslund N. 1985. Three-dimensional microscopy using a confocal laser scanning microscope. *Optics Letters* **10**:53–55. DOI: 10.1364/OL.10.000053
- Christenhusz MJM**, Byng JW. 2016. The number of known plant species in the world and its annual increase. *Phytotaxa* **261**:201–217. DOI: 10.11646/phytotaxa261.3.1
- Clark LH**, Harris WH. 1981. Observations on the root anatomy of rice (*oryza sativa l.*). *American Journal of Botany* **68**:154–161. DOI: 10.1002/j.1537-2197.1981.tb12374.x
- Cohen MF**. 2013. *An Introduction to Logic and Scientific Method*. Read Books Ltd.
- Daum B**, Kühlbrandt W. 2011. Electron tomography of plant thylakoid membranes. *Journal of Experimental Botany* **62**:2393–2402. DOI: 10.1093/jxb/err034
- De Neergaard E**, Lyshede OB, Gahoona TS, Care D, Hooker JE. 2000. *Anatomy and histology of roots and root-soil boundary*. Berlin, Germany: Springer Publishing
- De Oliveira Dal'Molin CG**, Quek LE, Saa PA, Nielsen, LK. 2015. A multi-tissue genome-scale metabolic modeling framework for the analysis of whole plant systems. *Frontiers in Plant Science* **6**:4. DOI: doi.org/10.3389/fpls.2015.00004
- Dölger J**, Rademaker H, Liesche J, Schulz A, Bohr T. 2014. Diffusion and bulk flow in phloem loading: A theoretical analysis of the polymer trap mechanism for sugar transport in plants. *Physical Review E* **90**:042704. DOI: 10.1103/PhysRevE.90.042704
- Ehlers K**, Kollmann R. 1996. Formation of branched plasmodesmata in regenerating solanum nigrum-protoplasts. *Planta* **199**:126–138. DOI: 10.1007/BF00196889
- Eom JS**, Chen LQ, Sosso D, Julius BT, Lin IW, Qu XQ, Braun DM, Frommer WB. 2015. Sweets, transporters for intracellular and intercellular sugar translocation. *Current Opinion in Plant Biology* **25**:53–62. DOI: 10.1016/j.pbi.2015.04.005
- El-Showk S**, Taylor-Teeple M, Helariutta Y, Brady SM. 2013. Gene regulatory networks during arabidopsis root vascular development. *International Journal of Plant Sciences* **174**:1090–1097. DOI: 10.1086/671449
- Evers JB**, Vos J, Fournier C, Andrieu B, Chelle M, Struik PC. 2005. Towards a generic architectural model of tillering in gramineae, as exemplified by spring wheat (*triticum aestivum*). *New Phytologist* **166**:801–812. DOI: 10.1111/j.1469-8137.2005.01337.x

Evert RF, Eichhorn SE. 2006. *Esau's Plant Anatomy: Meristems, Cells, and Tissues of the Plant Body: Their Structure, Function, and Development*, 3rd Ed. Hoboken, New Jersey, USA: John Wiley & Sons

Faulkner C. Plasmodesmata and the symplast. *Current Biology* **28**: R1365–R1381. DOI: 10.1016/j.cub.2018.11.004

Fisher DB, Cash-Clark CE. 2000. Sieve tube unloading and post-phloem transport of fluorescent tracers and proteins injected into sieve tubes via severed aphid stylets. *Plant Physiology* **123**:125–137. DOI: 10.1104/pp.123.1.125

Fisher DB, Oparka KJ. 1996. Post-phloem transport: Principles and problems. *Journal of Experimental Botany* **47**:1141–1154.

Fox RW, McDonald AT. 1985. *Introduction to Fluid Mechanics*, 3rd Ed. United States: John Wiley & Sons

Froelich DR, Mullendore DL, Jensen KH, Ross-Elliott T, Anstead JA, Thompson GA, Pélišsier HC, Knoblauch M. 2011. Phloem ultrastructure and pressure flow: Sieve-element-occlusion-related agglomerations do not affect translocation. *The Plant Cell* **23**:4428–4445. DOI: 10.1105/tpc.111.093179

Ganapathi TR, Suprasanna P, Rao PS, Bapat VA. 2004. Tobacco (*nicotiana tabacum* l.) –a model system for tissue culture interventions and genetic engineering. *Indian Journal of Biotechnology* **3**:171–184.

Giaquinta RT, Lin W, Sadler NL, Franceschi VR. 1983. Pathway of phloem unloading of sucrose in corn roots. *Plant Physiology* **72**:362–367. DOI: 10.1104/pp.72.2.362

Goff SA, Ricke D, Lan TH, Presting, G, Wang R, Dunn M, et al. 2002. A draft sequence of the rice genome (*oryza sativa* l. ssp *japonica*). *Science* **296**:92–100. DOI: 10.1126/science.1068275

Grinin LE. Production revolutions and the periodization of history. *Herald of the Russian Academy of Sciences* **77**:150–156. DOI: 10.1134/S1019331607020062

Haile MG, Kalkuhl M, von Braun J. 2016. Worldwide acreage and yield response to international price change and volatility: A dynamic panel data analysis for wheat, rice, corn, and soybeans. *American Journal of Agricultural Economics* **98**:172–190. DOI: 10.1093/ajae/aav013

Hammes UZ. 2016. Under pressure. *eLife* **5**:e15341. DOI: 10.7554/eLife.18435

Haupt-Herting S, Fock HP. 2002. Oxygen exchange in relation to carbon assimilation in water-stressed leaves during photosynthesis. *Annals of Botany* **89**:851–859. DOI: 10.1093/aob/mcf023

Heo JO, Roszak P, Furuta KM, Helariutta, Y. 2014. Phloem development: Current knowledge and future perspectives. *American Journal of Botany* **101**:1393–1402. DOI: 10.3732/ajb.1400197

Jensen KH, Mullendore DL, Holbrook NM, Bohr T, Knoblauch M, Bruus H. 2012. Modeling the hydrodynamics of phloem sieve plates. *Frontiers in Plant Science* **3**:151. DOI: 10.3389/fpls.2012.00151

Knoblauch M, Knoblauch J, Mullendore DL, Savage JA, Babst BA, Beecher SD, Dodgen AC, Jensen KH, Holbrook NM. 2017. Testing the münchen hypothesis of long distance phloem transport in plants. *eLife* **6**:e24125. DOI: 10.7554/eLife.24125

Knoblauch M, Peters WS. Forisomes, a novel type of Ca^{2+} -dependent contractile protein motor. *Cytoskeleton* **58**:137–142. DOI: 10.1002/cm.20006

Knoblauch M, Stubenrauch M, van Bel AJE, Peters WS. 2012. Forisome performance in artificial sieve tubes. *Plant, Cell & Environment* **35**:1419–1427. DOI: 10.1111/j.1365-3040.2012.02499.x

Knoblauch M, van Bel AJE. 1998. Sieve tubes in action. *The Plant Cell* **10**:35–50. DOI: 10.1105/tpc.10.1.35

Knoblauch M, Froelich DR, Pickard WF, Peters WS. 2014. Seorios business: Structural proteins in sieve tubes and their involvement in sieve element occlusion. *Journal of Experimental Botany* **65**:1879–1893. DOI: 10.1093/jxb/eru071

Knoblauch M, Vendrell M, de Leau E, Paterlini A, Knox K, Ross-Elliot T, Reinders A, Brockman SA, Ward J, Opara K. 2015. Multispectral phloem-mobile probes: Properties and applications. *Plant Physiology* **167**:1211–1220. DOI: 10.1104/pp.114.255414

Kragler F. 2013. Plasmodesmata: Intercellular tunnels facilitating transport of macromolecules in plants. *Cell and Tissue Research* **352**:49–58. DOI: 10.1007/s11120-013-9867-5

Kremer JR, Mastronarde DN, McIntosh JR. 1996. Computer visualization of three-dimensional image data using imod. *Journal of Structural Biology* **116**:71–76. DOI: 10.1006/jsbi.1996.0013

LaBarbera M. 1990. Principles of design of fluid transport in zoology. *Science* **249**:992–1000. DOI: 10.1126/science.2396104

Lucas WJ, Yoo BC, Kragler F. 2001. Rna as a long-distance information macromolecule in plants. *Nature Reviews Molecular Cell Biology* **2**:849–857.

Mastronarde DN. 1997. Dual-axis tomography: An approach with alignment methods that preserve resolution. *Journal of Structural Biology* **120**:343–352. DOI: 10.1006/jsbi.1997.3919

Mastronarde DN, Held SR. 2017. Automated tilt series alignment and tomographic reconstruction in imod. *Journal of Structural Biology* **197**:102–113. DOI: 10.1016/j.jsb.2016.07.011

- Maule AJ.** 2008. Plasmodesmata: Structure, function and biogenesis. *Current Opinion in Plant Biology* **11**:680–686. DOI: 10.1016/j.pbi.2008.08.002
- Maule AJ**, Benitez-Alfonso Y, Faulkner C. 2011. Plasmodesmata – membrane tunnels with attitude. *Current opinion in Plant Biology* **14**:683–690. DOI: 10.1016/j.pbi.2011.07.007
- Mellinger MV**, McNaughton SJ. 1975. Structure and function of successional vascular plant communities in central new york. *Ecological Monographs* **45**:161–182. DOI: 10.2307/1942405
- Meschini S.** 2017. Correlative microscopy in life and materials sciences. *European Journal of Histochemistry* **61**:1–8. DOI: 10.4081/ejh.2017.2864
- Morton AG.** 1981. *History of Botanical Science. An account of the development of botany from ancient times to the present day*. London, UK: Academic Press
- Mullendore DL**, Froelich DR, Beecher S, Ross-Elliott TJ, Knoblauch J, Knoblauch M. 2015. Investigation of structure-function relationship of long-distance transport in plants: New imaging tools to answer old questions. *Microscopy and Microanalysis* **21**:1491–1492. DOI: 10.1017/S1431927615008235
- Mullendore DL**, Windt CW, As HV, Knoblauch M. 2010. Sieve tube geometry in relation to phloem flow. *The Plant Cell* **22**:579–593. DOI: 10.1105/tpc.109.070094
- Münch E.** 1930. *Die stoffbewegungen der pflanze*. Jena, Germany: G. Fisher
- Oparka KJ**, Duckett CM, Prior DAM, Fisher DB. 1994. Real-time imaging of phloem unloading in the root tip of arabidopsis. *The Plant Journal* **6**:759–766. DOI: 10.1046/j.1365-313X.1994.6050759.x
- Oparka KJ.** 2005. Plasmodesmata: Annual Plant Reviews, Volume 14. Oxford, UK: Blackwell Publishing
- Oparka KJ**, Turgeon R. 1999. Sieve elements and companion cells-traffic control centers of the phloem. *The Plant Cell* **11**:739–750. DOI: 10.2307/3870896
- Patrick JW.** 1997. Phloem unloading: Sieve element unloading and post-sieve element transport. *Annual Review of Plant Physiology and Plant Molecular Biology* **48**:191–222. DOI: 10.1146/annurev.applant.48.1.191
- Patrick JW.** 2013. Does don fisher's high-pressure manifold model account for phloem transport and resource partitioning? *Frontiers in Plant Science* **4**:184. DOI: 10.3389/fpls.2013.00184
- Peters WS**, van Bel AJE, Knoblauch M. 2006. The geometry of the forisome-sieve element-sieve plate complex in the phloem of vicia faba l. leaflets. *Journal of Experimental Botany* **57**:3091–3098. DOI: 10.1093/jxb/erl072

- Porter KR**, Kallman F. 1952. The properties and effects of osmium tetroxide as a tissue fixative with special reference to its use for electron microscopy. *Experimental Cell Research* **4**:127–141. DOI: 10.1016/0014-4827(53)90195-5
- Pozrikidis C**. 2011. *Introduction to Theoretical and Computational Fluid Dynamics*. Oxford, UK: Oxford University Press.
- Radford JE**, Vesk M, Overall RL. 1998. Callose deposition at plasmodesmata. *Protoplasma* **201**:30–37. DOI: 10.1007/BF01280708
- Raven JA**. 2003. Long-distance transport in non-vascular plants. *Plant, Cell and Environment* **26**:73–85. DOI: 10.1046/j.1365-3040.2003.00920.x
- Rennie EA**, Turgeon R. 2009. A comprehensive picture of phloem loading strategies. *Proceedings of the National Academy of Sciences* **33**:14162–14167. DOI: 10.1073/pnas.0902279106
- Roser M**, Ortiz-Ospina E. 2017. World population growth. Published online at OurWorldInData.org
- Roy J**, Saugier B, Mooney HA. 2001. *Terrestrial Global Productivity*. San Diego, California, USA: Academic Press
- Savage JA**, Beecher SD, Clerx L, Gersony JT, Knoblauch J, Losada JM, Jensen KH, Knoblauch M, Holbrook NM. 2017. Maintenance of carbohydrate transport in tall trees. *Nature Plants* **3**:965–972. DOI: 10.1038/s41477-017-0064-y
- Savary S**, Ficke A, Aubertot JN, Hollier C. 2012. Crop losses due to diseases and their implications for global food production losses and food security. *Food Security* **4**:519–537. DOI: 10.1007/s12571-012-0200-5
- Sawaguchi A**, Ide S, Goto Y, Kawano JI, Oinuma T, Suganuma T. 2001. A simple contrast enhancement by potassium permanganate oxidation for lowicryl k4m ultrathin sections prepared by high pressure freezing/freeze substitution. *Journal of Microscopy* **201**:77–83. DOI: 10.1046/j.1365-2818.2001.00787.x
- Schermelleh L**, Heintzmann R, Leonhardt H. 2010. A guide to super-resolution fluorescence microscopy. *Journal of Cell Biology* **190**:165. DOI: 10.1083/jcb.201002018
- Schreiber L**, Hartmann K, Scrabs M, Zeier J. Apoplastic barriers in roots: Chemical composition of endodermal and hypodermal cell walls. *Journal of Experimental Botany* **50**:1267–1280. DOI: 10.1093/jxb/50.337.1267
- Sjolund RD**. 1997. The phloem sieve element: a river runs through it. *The Plant Cell* **9**:1137–1146. DOI: 10.1105/tpc.9.7.1137

- Stanfield RC**, Schulte PJ, Randolph KE, Hacke UG. 2018. Computational models evaluating the impact of sieve plates and radial water exchange on phloem pressure gradients. *Plant, Cell & Environment* **42**:466–479. DOI: 10.1111/pce.13414
- Stempak JG**, Ward RT. 1964. An improved staining method for electron microscopy. *Journal of Cell Biology* **22**:697–701.
- Sumner J**. 2000. *The Natural History of Medicinal Plants*. New York, USA: Timber Press.
- Stern KR**, Jansky S, Bidlack JE, Bidlack J. 2003. *Introductory Plant Biology*. London, UK: McGraw-Hill Higher Education
- Talbot MJ**, White RG. 2013. Methanol fixation of plant tissue for scanning electron microscopy improves preservation of tissue morphology and dimensions. *Plant Methods* **9**:36. DOI: 10.1186/1746-4811-9-36
- Terashima I**, Fujita T, Inoue T, Chow WS, Oguchi R. 2009. Green light drives leaf photosynthesis more efficiently than red light in strong white light: Revisiting the enigmatic question of why leaves are green. *Plant and Cell Physiology* **50**:684–697. DOI: 10.1093/pcp/pcp034
- Toyooka K**, Kang Byung-Ho. 2014. Reconstructing plant cells in 3d by serial section electron tomography. *Plant Cell Morphogenesis – Methods in Molecular Biology* **1080**:159–170. DOI: 10.1007/978-1-62703-643-6_13
- Turgeon R**, Wolf S. 2009. Phloem transport: Cellular pathways and molecular trafficking. *Annual Review of Plant Biology* **60**:207–221. DOI: 10.1146/annurev.arplant.043008.092045
- van Bel AJE**, Knoblauch M. 2000. Sieve element and companion cell: the story of the comatose patient and the hyperactive nurse. *Functional Plant Biology* **27**:477–487. DOI: 10.1071/PP99172
- Zhang C**, Han L, Slewinski TL, Turgeon R. 2014. Symplastic phloem loading in poplar. *Plant Physiology* **166**:306–313. DOI: 10.1104/pp.114.245845